Six Degrees of Freedom Mobile Inductive Power Transfer by Crossed Dipole Tx and Rx Coils

Bo H. Choi, *Student Member, IEEE*, Eun S. Lee, *Student Member, IEEE*, Yeong H. Sohn, *Student Member, IEEE*, Gi C. Jang, *Student Member, IEEE*, and Chun T. Rim, *Senior Member, IEEE*

***Abstract*—Crossed dipole coils for the wide-range 3-D omnidirectional inductive power transfer (IPT) are proposed. Free positioning of a plane receiving (Rx) coil is obtained for an arbitrary direction within 1m from a plane transmission (Tx) coil. Both the Tx and Rx coils consists of crossed dipole coils with an orthogonal phase difference; hence, a rotating magnetic field is generated from the Tx, which enables the Rx to receive power vertically or horizontally. Thus, the 3-D omnidirectional IPT is first realized for both the plate type Tx and Rx coils, which is crucial for practical applications, where volumetric coil structure is highly prohibited. This optimized configuration of coils has been obtained through a general classification of power transfer and searching for mathematical constraints on multi-D omnidirectional IPT. Conventional loop coils are thoroughly analyzed, and verified to be inadequate for the plate-type omnidirectional IPT in this paper. Simulation-based design of the proposed crossed dipole coils for a uniform magnetic field distribution is provided, and the 3-D omnidirectional IPT is experimentally verified by prototype Rx coils for a wireless power- zone of 1 m^3 with a prototype Tx coil of 1 m^2 at an operating frequency of 280 kHz, meeting the power matters alliance. The maximum overall efficiency was 33.6% when the input power was 100 W.**

***Index Terms*—Degree of freedom, dipole coil resonance system, omnidirectional IPT, ubiquitous power, wireless power transfer (WPT).**

I. Introduction

THE methods of power transfer (PT) for various sources and loads have evolved, since the advent of electricity in the 19th century [1]–[58]. In general, PTs can be classified to the stationary and mobile depending on the movement of loads as shown in Fig. 1. The stationary PT (SPT) includes the fixed SPT of firmly unchanged configuration of power systems and the detachable SPT of variable configuration of power systems, which again can be classified into plugged SPT and wireless SPT. To cope with the strong demands for mobility of receiving (Rx) loads, various mobile PTs (MPTs) have been proposed, which can be further classified to close MPT and remote MPT depending on the range. Among the close MPTs, the inductive PT (IPT) has been used widely due to its high PT capability at relatively low frequency, whereas the capacitive PT is not so commonly used due to its high operating frequency and small PT distance [1]–[2]. Note that the conductive PT was widely used for a century as a practical means for MPT until the advent of IPT. Among the remote MPTs, radio frequency (RF) PT and optical PT have been researched to extend the range limit of other PTs [3]–[4]. The wired PT can provide power over a flexibly long distance if properly designed [5], [6]. As depicted in Fig. 1, the wireless PT (WPT) embraces not only the IPT, capacitive PT, RF PT, and optical PT, but also the wireless SPT. In the era of ubiquitous, the IPT is the most widely used among the WPTs [8]–[58]. More mobile devices, home appliances, industry sensors, and electric vehicle (EV) chargers are becoming wireless due to their convenience, safety against electric shock, cleanness, and competitive power efficiency and price. Eventually, most devices including wearable devices, ubiquitous sensors, and smart cars will merge to the internet of things (IoT), and WPT shall play a significantly important role in the realization of IoT, which includes compact communication devices, sensors, and power sources.

As a power source of IoT, the degrees of freedom (DoF) of an Rx load in position and rotation are of paramount importance as shown in Fig. 2. The 6 DoF in three-dimensional (3-D) space are composed of the position vector $\overrightarrow{P}\,(x, y, z)$ and rotation vector $\overrightarrow{R}\,(\theta_x, \theta_y, \theta_z)$ in this paper, where the rotation of an Rx normal vector $\overrightarrow{n}$ is defined as pitch (θ_x), roll (θ_y), and yaw (θ). To ensure the full mobility of an Rx load, two characteristics of "free positioning" and "omnidirectional powering" should be guaranteed, which corresponds to $\overrightarrow{P}\,(x, y, z)$ and $\overrightarrow{R}\,(\theta_x, \theta_y, \theta_z)$, respectively. Confining the discussions in this paper to IPT only, the free positioning of an Rx coil is obtained by an evenly distributed magnetic field intensity of a transmission (Tx) coil, while the omnidirectional powering of an Rx coil is guaranteed by nonzero induced load voltage over any rotation angles. To cope with the free-positioning and omnidirectional powering problems, multiple planar coil structures have been proposed in wireless charging pad applications [8]–[11]; however, only lateral free positioning with one rotation over a Tx coil surface can be obtained at near distance. To achieve the omnidirectional powering, multiple coils are combined in perpendicular to allow two or three rotations in a 3-D space [12]–[18]; however, volumetric coil structures are hardly implementable to mobile devices in practice. On the other hand,

Manuscript received May 10, 2015; accepted June 19, 2015. Date of publication June 24, 2015; date of current version November 30, 2015. This paper was presented in part at the IEEE Energy Conversion Congress and Exposition, Montreal, Canada, September 20–24, 2015. This work was supported by an R&D grant of rehabilitation services by the Korea National Rehabilitation Center Research Institute, Ministry of Health and Welfare (2014002). Recommended for publication by Associate Editor S.Y. Hui.

B. H. Choi, E. S. Lee, G. C. Jang, and C. T. Rim are with the Department of Nuclear and Quantum Engineering, Korea Advanced Institute of Science and Technology, Daejeon 305-755, Korea (e-mail: bohwan@kaist.ac.kr; eunsoo86@kaist.ac.kr; gcjang@kaist.ac.kr; ctrim@kaist.ac.kr).

Y. H. Sohn is with the Department of Electrical Engineering, Korea Advanced Institute of Science and Technology, Daejeon 305-755, Korea (e-mail: sonyh216@kaist.ac.kr).

Color versions of one or more of the figures in this paper are available online at http://ieeexplore.ieee.org.

Digital Object Identifier 10.1109/TPEL.2015.2449290

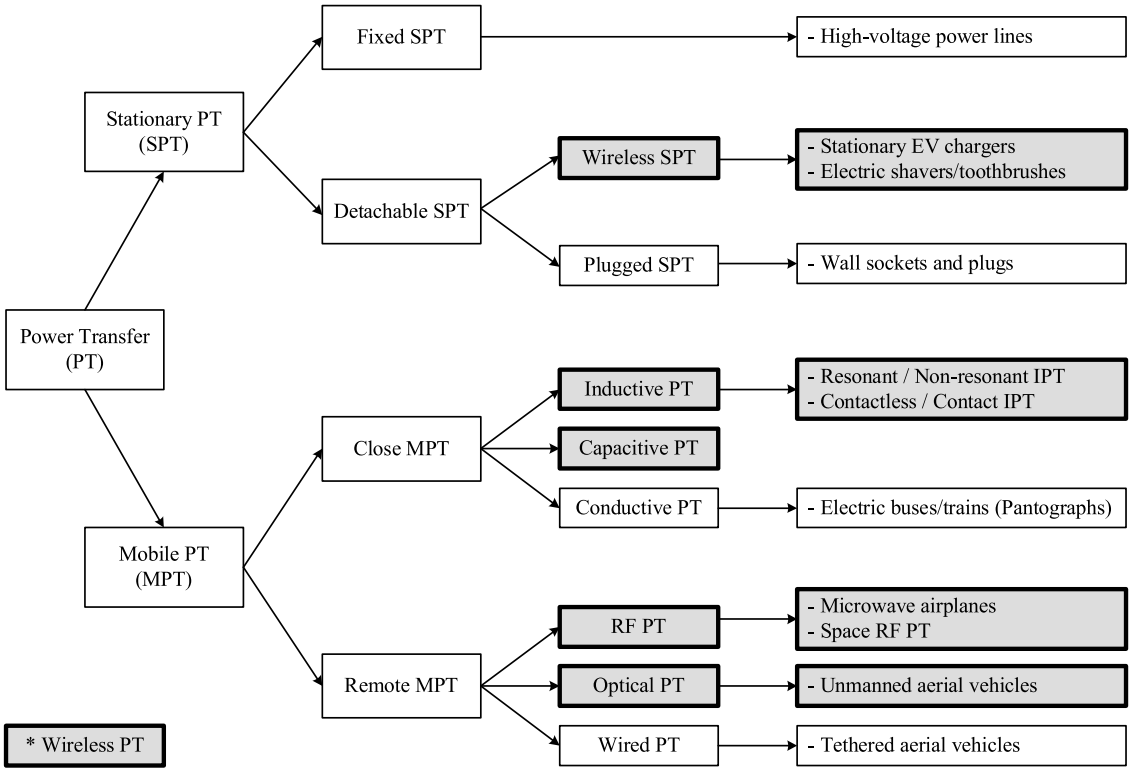

Fig. 1. Proposed general category of PTs.

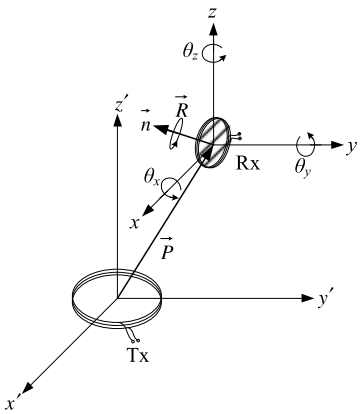

Fig. 2. Definition of 6 DoF of an Rx load w.r.t. Tx in 3-D space.

long- and narrow-shaped dipole coils with ferrite cores were used to achieve a dimension reduction in coil structures, where the overall superiority of dipole coils for a long-distance power delivery over loop coils has been verified in [19] and [20].

As a candidate of IPTs solving both free-positioning and omnidirectional powering, new crossed dipole Tx and Rx coils having 6 DoF with DQ rotating magnetic field are proposed in this paper, as shown in Fig. 3. Two crossed dipole coils with orthogonal phase differences generate a rotating magnetic field to provide the Rx coil with the highest DoF. The plane geometry of the proposed coils can resolve the chronic installation problems associated with the volumetric coil structures in conventional omnidirectional IPTs. The operating frequency of the proposed Tx and Rx coils was selected as 280 kHz, meeting the international guideline of power matters alliance (PMA). Simulation-based design of the proposed crossed dipole coils for a uniform magnetic field distribution is provided, and the 3-D omnidirectional IPT is experimentally verified by prototype Rx coils for a wireless power- zone of 1 m^3 with a prototype Tx coil of 1 m^2.

The rest of this paper is organized as follows. Section II presents analyses on omnidirectional powering IPT coil structures, such as loop coils and dipole coils. Section III shows the characteristics of the proposed crossed dipole coils having 6 DoF with DQ rotating magnetic field based on analyses and simulations. Section IV presents experimental verifications of the omnidirectional powering using fabricated Tx and Rx coils. The conclusions are provided in Section V.

II. Evaluation of DoF on Various PTs

In this section, various PTs in Fig. 1 are comparatively evaluated according to the DoF of the Rx load in position and rotation. As listed in Table I, the PTs are categorized into seven configurations, as shown in Fig. 4, according to the proposed classification of Fig. 1. Neither fixed nor detachable SPTs allow any mobility of Rx load in general. For example, a high-voltage power line is fixed at metal towers and a wall socket does not allow any DoF of the connected wall plug, as shown in Fig. 4(a) and (b). On the other hand, at least one DoF in position or rotation is guaranteed for MPTs in general to ensure the mobility of an Rx load. As an example of IPTs, a dipole coil resonance system is

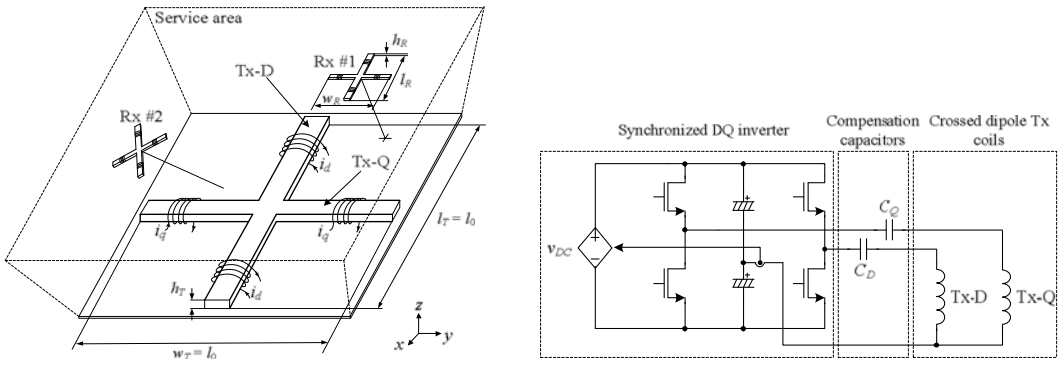

(a) (b)

Fig. 3. Proposed crossed dipole coils for 6 DoF. (a) Overall Tx and Rx coil configuration. (b) Circuit diagram showing series resonance circuits.

TABLE I
DOF OF PT ACCORDING TO THE PROPOSED SEVEN CLASSIFICATIONS

PT methods		Maximum allowable number of DoF		Remarks
		Position (x, y, z)	Rotation (θ_x, θ_y, θ_z)	
SPT	Fixed SPT	0	0	Wired
	Detachable SPT	0	0	Wired/Wireless
MPT	IPT	3	3	Wireless
	Capacitive PT	2	1	Wireless
	Conductive PT	1	0	Wired
	RF/Optical PT	3	3	Wireless
	Wired PT	3	3	Wired

illustrated in Fig. 4(c). The maximum allowable DoF for both the position and rotation is three when an omnidirectional Tx coil or Rx coil is used, and this will be discussed in detail in this paper. The capacitive PTs using two capacitive-coupled metal plates, however, can transfer power only when the two metal plates are located in parallel, as shown in Fig. 4(d); hence, the maximum DoF of the capacitive PTs is two for position and one for rotation, respectively. An example of conductive PT is the pantograph of a tram, which collects power through a contact with an overhead wire; thus, the maximum DoF in position and rotation are one and zero, respectively, as shown in Fig. 4(e). Note that the heading of a tram has three DoF in position and rotation, but a rail is fixed and not arbitrarily changeable. A laser power transmission, as depicted in Fig. 4(f), can support all DoF of an Rx load in position and rotation over an arbitrary 3-D space. A tethered aerial vehicle connected with a flexible power line also has 6 DoF within the range of an available power line as shown in Fig. 4(g).

III. OMNIDIRECTIONAL WPTS BY LOOP COILS

A. Analysis on Rx Coils Under Evenly Distributed Magnetic Flux Density

As the IPT has been identified as a candidate for omnidirectional powering, the DoF for three rotations θ_x, θ_y, and θ_z in IPTs are evaluated for loop coil structures first, which have been widely used for ubiquitous powering [12]–[18]. While the omnidirectional IPT was experimentally verified in [12]–[18], the omnidirectional powering conditions in the IPT are theoretically analyzed in detail in this paper. The minimum physical dimensions of Tx and Rx coils allowing arbitrary rotations in 3-D position are also investigated. It is assumed that the Rx coil is quite small compared to the Tx coil and that the magnetic field intensity from the Tx coil is evenly distributed for a specified 3-D space; thus, the free positioning of the Rx coil is inherently guaranteed. The number of Tx coils, which is orthogonal to each other, is defined as m_T, and that of Rx coils is defined as m_R, respectively. For example, a single-loop coil or a dipole coil corresponds to $m_T = 1$, and two orthogonal loop coils correspond to $m_T = 2$ when they are used for Tx purpose.

Considering typical ubiquitous powering coil structures, it is assumed that the maximum m_R is three and all symmetric Rx coils, namely Rx-1, Rx-2, and Rx-3, are orthogonal to each other as shown in Fig. 5. The induced voltage of Rx coils in the steady state, which has area A_{Rx} and number of turns N_{Rx}, is calculated for an arbitrary rotation when the evenly distributed sinusoidal magnetic flux density vector $\overrightarrow{\boldsymbol{B}}_0$ of phasor form, having angular frequency of ω_s, is externally applied to the 3-D space. Throughout this paper, bold letters are used to represent phasors and an upper arrow is used to represent a vector throughout this paper. The magnetic flux $\boldsymbol{\varphi}_1$ of phasor form, penetrating Rx-1, can be determined as follows:

$$\begin{aligned}\boldsymbol{\varphi}_1 &\equiv \int_S \overrightarrow{\boldsymbol{B}}_0 \cdot d\overrightarrow{S} \cong A_{Rx}\overrightarrow{\boldsymbol{B}}_0 \cdot \overrightarrow{n}_1 \\ &= A_{\mathrm{Rx}}\left(n_{1x}B_x\angle\alpha_x + n_{1y}B_y\angle\alpha_y + n_{1z}B_z\angle\alpha_z\right) \quad (1)\end{aligned}$$

where $\overrightarrow{\boldsymbol{B}}_0$ and $\overrightarrow{n}_1$ are represented as a phasor vector and a normalized scalar vector, respectively, as

$$\overrightarrow{\boldsymbol{B}}_0 \equiv (B_x\angle\alpha_x, B_y\angle\alpha_y, B_z\angle\alpha_z) \quad (2a)$$

$$\overrightarrow{n}_1 \equiv (n_{1x}, n_{1y}, n_{1z}). \quad (2b)$$

Then, the induced Rx coil voltage $\boldsymbol{V}_1$ for Rx-1 of phasor form can be determined by Faraday's law from (1) as follows:

$$\begin{aligned}\boldsymbol{V}_1 &= j\omega_s N_{\mathrm{Rx}}\boldsymbol{\varphi}_1 \\ &= jV_m\left(n_{1x}B_x\angle\alpha_x + n_{1y}B_y\angle\alpha_y + n_{1z}B_z\angle\alpha_z\right) \\ &\quad \because V_m \equiv \omega_s N_{\mathrm{Rx}}A_{\mathrm{Rx}}. \quad (3)\end{aligned}$$

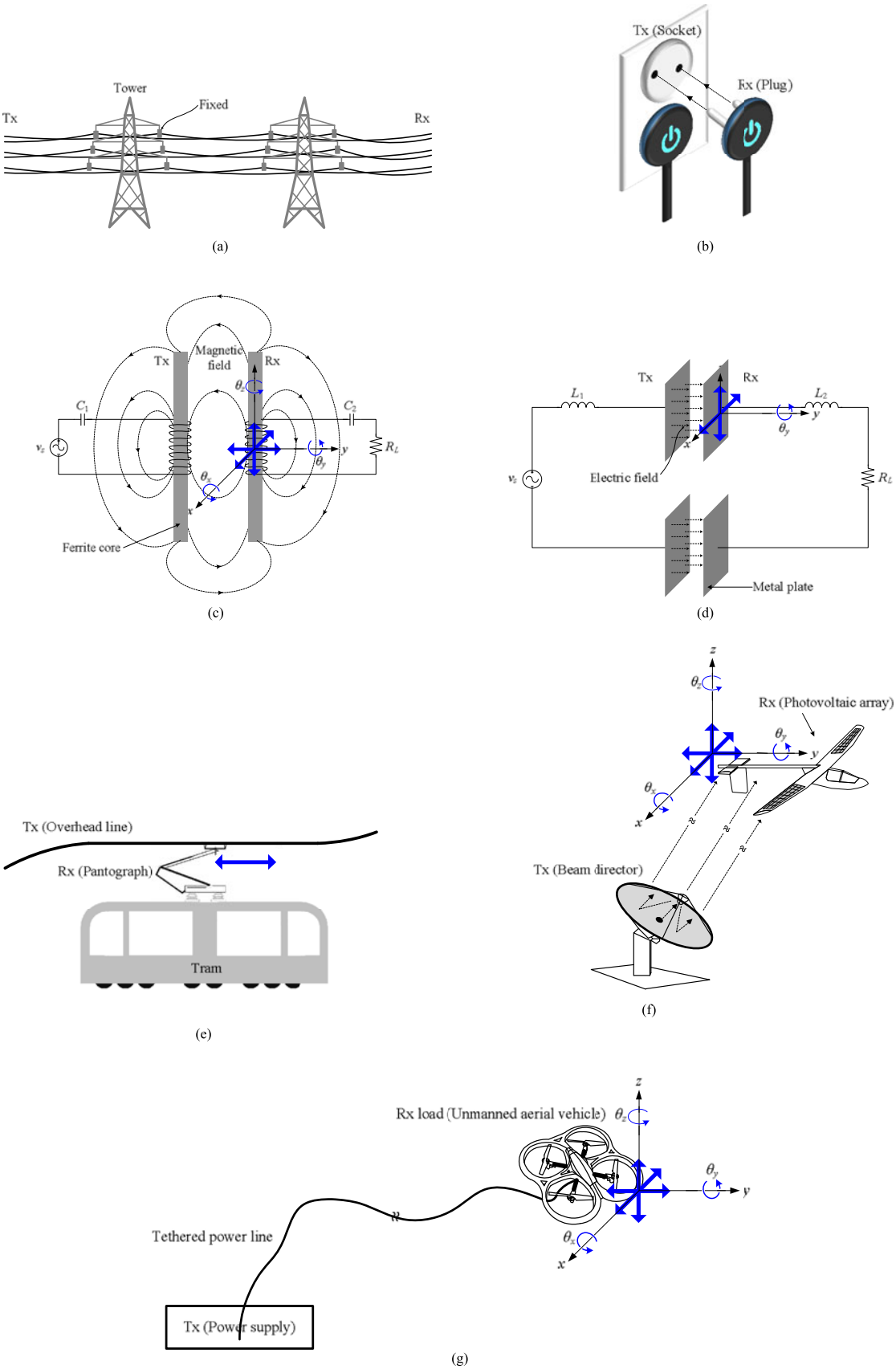

Fig. 4. Examples of PTs with respect to a 6 DoF viewpoint. "$m_1P - m_2R$" means the DoF of position and rotation are m_1 and m_2, respectively. (a) Fixed SPT: High-voltage power line and tower (0P-0R). (b) Detachable SPT: A set of wall socket and plug (0P-0R). (c) PT: Dipole coil resonant system (3P-3R). (d) Capacitive PT (2P-1R). (e) Conductive PT: Pantograph with tram (1P-0R). (f) RF/Optical PT: Laser power transmission (3P-3R). (g) Wired PT: Tethered aerial vehicle (3P-3R).

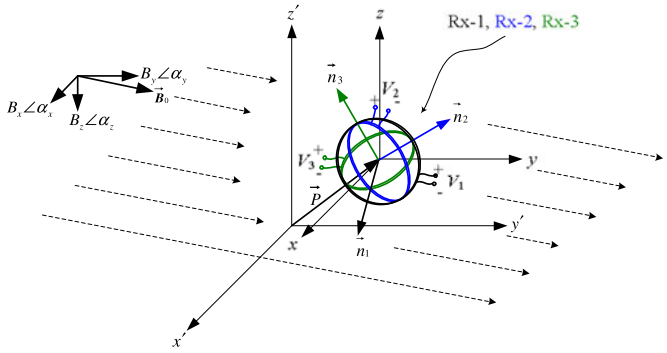

Fig. 5. Three Rx loop coils under the evenly distributed magnetic flux density.

In (3), $\boldsymbol{V}_1$ can be determined for an arbitrary direction defined by $\overrightarrow{n}_1 \equiv (n_{1x}, n_{1y}, n_{1z})$, which is determined by a transformation matrix R_{ijk} [59] and x-directional normal vector $\overrightarrow{n}_{10}$ as follows:

$$\begin{bmatrix} n_{1x} \\ n_{1y} \\ n_{1z} \end{bmatrix} = R_i \quad R_j \quad R_k \begin{bmatrix} 1 \\ 0 \\ 0 \end{bmatrix} = R_{ijk} \begin{bmatrix} 1 \\ 0 \\ 0 \end{bmatrix}$$

$$\text{for } R_{ijk} \equiv R_i \quad R_j \quad R_k \tag{4}$$

where $\overrightarrow{n}_1 \equiv (1,0,0)$ is a reference vector of $\overrightarrow{n}_1$ in this paper before any rotating of Rx-1. Note that R_{ijk} is defined as a matrix multiplication of R_i, R_j, and R_k when "*ijk*" is a permutation of a set {*x*, *y*, *z*}, namely "*xyz*," "*xzy*," "*yxz*," "*yzx*," "*zxy*," and "*zyx*." For simplicity, R_{zyx} is selected among R_{ijk} in this paper, which denotes a sequential rotation of Rx-1 w.r.t. pitch (θ_x), roll (θ_y), and yaw (θ_z), where R_x, R_y, and R_z are defined as follows [59]:

$$R_x = \begin{bmatrix} 1 & 0 & 0 \\ 0 & \cos\theta_x & -\sin\theta_x \\ 0 & \sin\theta_x & \cos\theta_x \end{bmatrix} \tag{5a}$$

$$R_y = \begin{bmatrix} \cos\theta_y & 0 & \sin\theta_y \\ 0 & 1 & 0 \\ -\sin\theta_y & 0 & \cos\theta_y \end{bmatrix} \tag{5b}$$

$$R_z = \begin{bmatrix} \cos\theta_z & -\sin\theta_z & 0 \\ \sin\theta_z & \cos\theta_z & 0 \\ 0 & 0 & 1 \end{bmatrix}. \tag{5c}$$

Applying (4) to (5), $\boldsymbol{V}_1$ in (3) becomes as follows:

$$\begin{aligned} \boldsymbol{V}_1|_{\overrightarrow{n}=\overrightarrow{n}_1} &= jV_m \left(\cos\theta_y \cos\theta_z B_x\angle\alpha_x \right. \\ &\quad \left. + \cos\theta_y \sin\theta_z B_y\angle\alpha_y - \sin\theta_y B_z\angle\alpha_z\right). \end{aligned} \tag{6}$$

Expanding the discussion in (1)–(3) to the multiple orthogonal Rx coils, the $\boldsymbol{V}_2$ and $\boldsymbol{V}_3$, which are the induced Rx coil voltages of Rx-2 and Rx-3, respectively, can be derived, as follows:

$$\boldsymbol{V}_2 = jV_m \left(n_{2x}B_x\angle\alpha_x + n_{2y}B_y\angle\alpha_y + n_{2z}B_z\angle\alpha_z\right) \tag{7a}$$

$$\boldsymbol{V}_3 = jV_m \left(n_{3x}B_x\angle\alpha_x + n_{3y}B_y\angle\alpha_y + n_{3z}B_z\angle\alpha_z\right) \tag{7b}$$

where the normal vectors of each coil are defined as $\overrightarrow{n}_2 \equiv (n_{2x}, n_{2y}, n_{2z})$ and $\overrightarrow{n}_3 \equiv (n_{3x}, n_{3y}, n_{3z})$.

In a similar fashion to (4)–(6), (7) becomes as follows for the y- and z-directional reference vectors of $\overrightarrow{n}_{20} \equiv (0,1,0)$ and $\overrightarrow{n}_{30} \equiv (0,0,1)$, respectively, in this paper:

$$\begin{aligned} &\boldsymbol{V}_2|_{\overrightarrow{n}=\overrightarrow{n}_2} \\ &= jV_m \left\{(\sin\theta_x \sin\theta_y \cos\theta_z - \cos\theta_x \sin\theta_z) B_x\angle\alpha_x \right. \\ &\quad + (\sin\theta_x \sin\theta_y \sin\theta_z + \cos\theta_x \cos\theta_z) B_y\angle\alpha_y \\ &\quad \left. + \sin\theta_x \cos\theta_y B_z\angle\alpha_z\right\} \end{aligned} \tag{8a}$$

$$\begin{aligned} &\boldsymbol{V}_3|_{\overrightarrow{n}=\overrightarrow{n}_3} \\ &= jV_m \left\{(\cos\theta_x \sin\theta_y \cos\theta_z + \sin\theta_x \sin\theta_z) B_x\angle\alpha_x \right. \\ &\quad + (\cos\theta_x \sin\theta_y \sin\theta_z - \sin\theta_x \cos\theta_z) B_y\angle\alpha_y \\ &\quad \left. + \cos\theta_x \cos\theta_y B_z\angle\alpha_z\right\}. \end{aligned} \tag{8b}$$

In the following sections, three possible configurations of a few Tx and Rx coils guaranteeing the omnidirectional powering are evaluated in detail based on the above analysis. The evaluation results for the first two coil configurations of "1Tx-3Rx" having $(m_T, m_R) = (1,3)$ and "3Tx-1Rx" having $(m_T, m_R) = (3,1)$ match well with the results [12]–[18], which experimentally verified the omnidirectional powering characteristics. "2Tx-2Rx" configuration having $(m_T, m_R) = (2,2)$ is first proposed in this paper, and also guarantees omnidirectional wireless powering, i.e., nonzero induced load voltage over any rotation angles.

B. Single Tx Coil and Triple Rx Coils (1Tx-3Rx)

It is well known that a set of triple orthogonal Rx coils enables us to achieve omnidirectional powering with a single Tx coil, i.e., $(m_T, m_R) = (1,3)$ [14]–[18]. Two possible coil configurations achieving $(m_T, m_R) = (1,3)$ are illustrated in Fig. 6(a) and (b). As shown in Fig. 6(b), a pair of loop coils facing each other, namely "Tx-1a and Tx-1b," is used instead of the single-loop coil in Fig. 6(a) for higher uniformity of magnetic flux. For simplicity, it is assumed that the magnetic flux density from all the Tx coil in Fig. 6 has only x-directional components, i.e., $B_x \neq 0, B_y = B_z = 0$. Then, the Rx coil voltages in (6) and (8) can be rewritten as follows:

$$\boldsymbol{V}_1|_{\overrightarrow{n}=\overrightarrow{n}_1} = jV_m \cos\theta_y \cos\theta_z B_x\angle\alpha_x \tag{9a}$$

$$\begin{aligned} \boldsymbol{V}_2|_{\overrightarrow{n}=\overrightarrow{n}_2} &= jV_m \left(\sin\theta_x \sin\theta_y \cos\theta_z \right. \\ &\quad \left. - \cos\theta_x \sin\theta_z\right) B_x\angle\alpha_x \end{aligned} \tag{9b}$$

$$\begin{aligned} \boldsymbol{V}_3|_{\overrightarrow{n}=\overrightarrow{n}_3} &= jV_m \left(\cos\theta_x \sin\theta_y \cos\theta_z \right. \\ &\quad \left. + \sin\theta_x \sin\theta_z\right) B_x\angle\alpha_x. \end{aligned} \tag{9c}$$

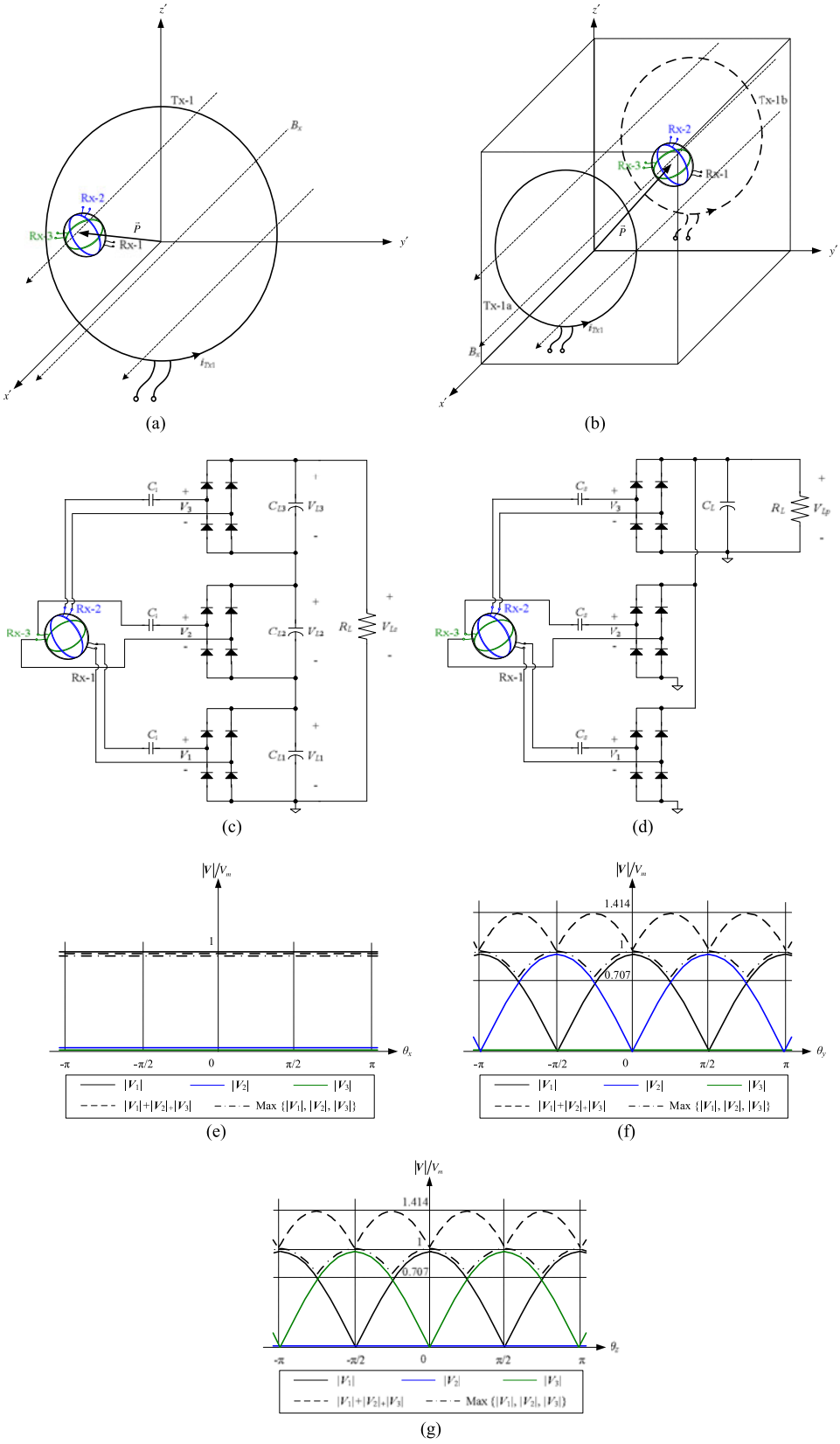

Fig. 6. 1Tx-3Rx coil configurations and their normalized values of induced Rx coil voltages when (m_T, m_R) is (1, 3). (a) 1Tx-3Rx coil configuration. (b) 1Tx-3Rx coil configuration, where a pair of loop coils facing each other is used for Tx. (c) Series connection of the Rx coils and their rectifiers. (d) Parallel connection of the Rx coils and their rectifiers. (e) Induced Rx coil voltages w.r.t. θ_x rotation. (f) Induced Rx coil voltages w.r.t. θ_y rotation. (g) Induced Rx coil voltages w.r.t. θ_z rotation.

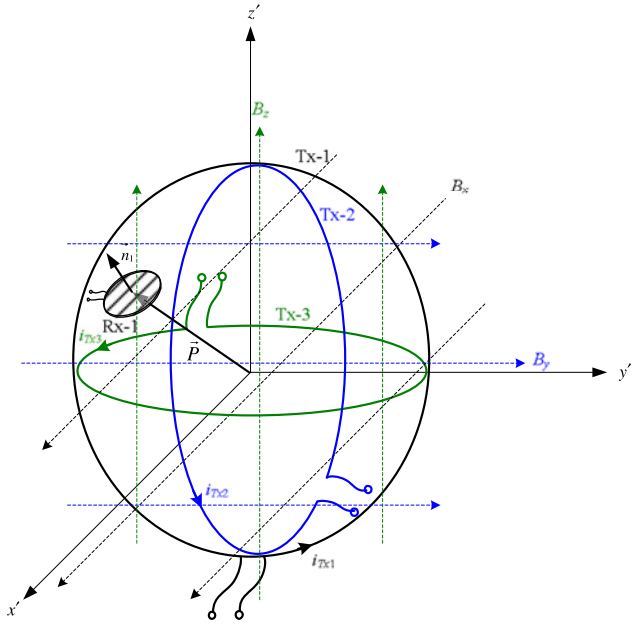

(a)

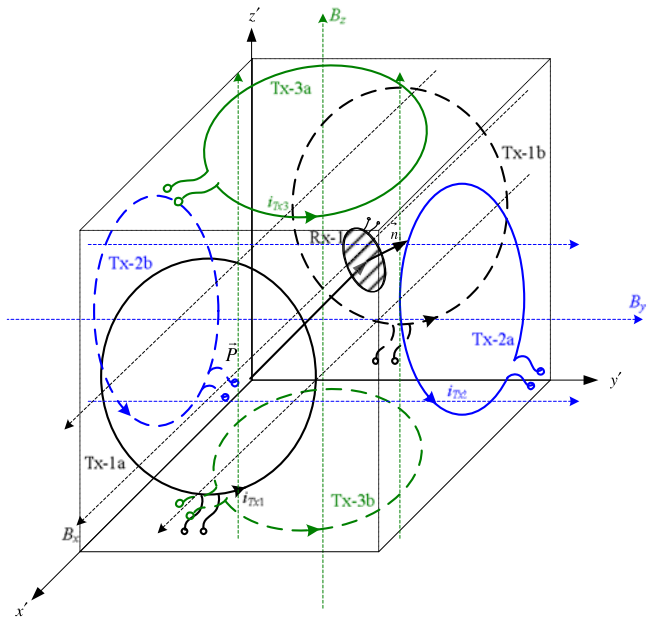

(b)

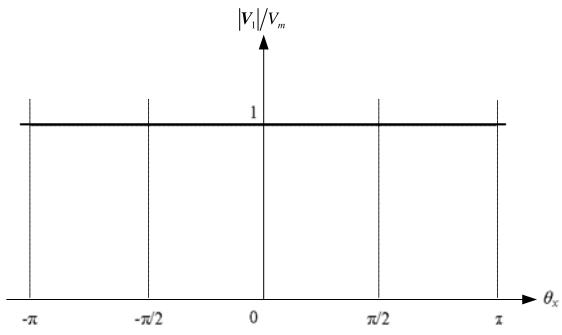

(c)

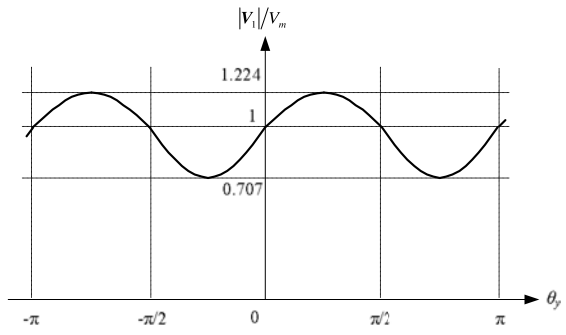

(d)

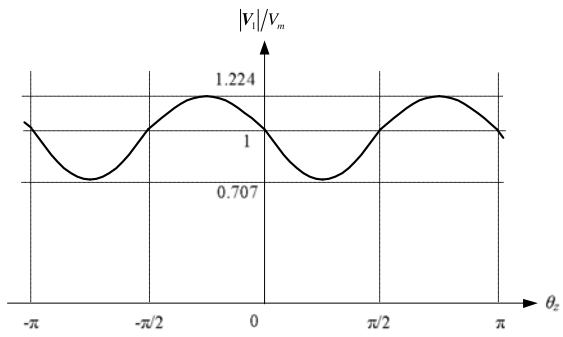

(e)

Fig. 7. 3Tx-1Rx coil configurations and their normalized values of induced Rx coil voltages when (m_T, m_R) is (3, 1). (a) 3Tx-1Rx coil configuration. (b) 3Tx-1Rx coil configuration, where a pair of loop coils facing each other is used for Tx. (c) Induced Rx coil voltage w.r.t. θ_x rotation. (d) Induced Rx coil voltage w.r.t. θ_y rotation. (e) Induced Rx coil voltage w.r.t. θ_z rotation.

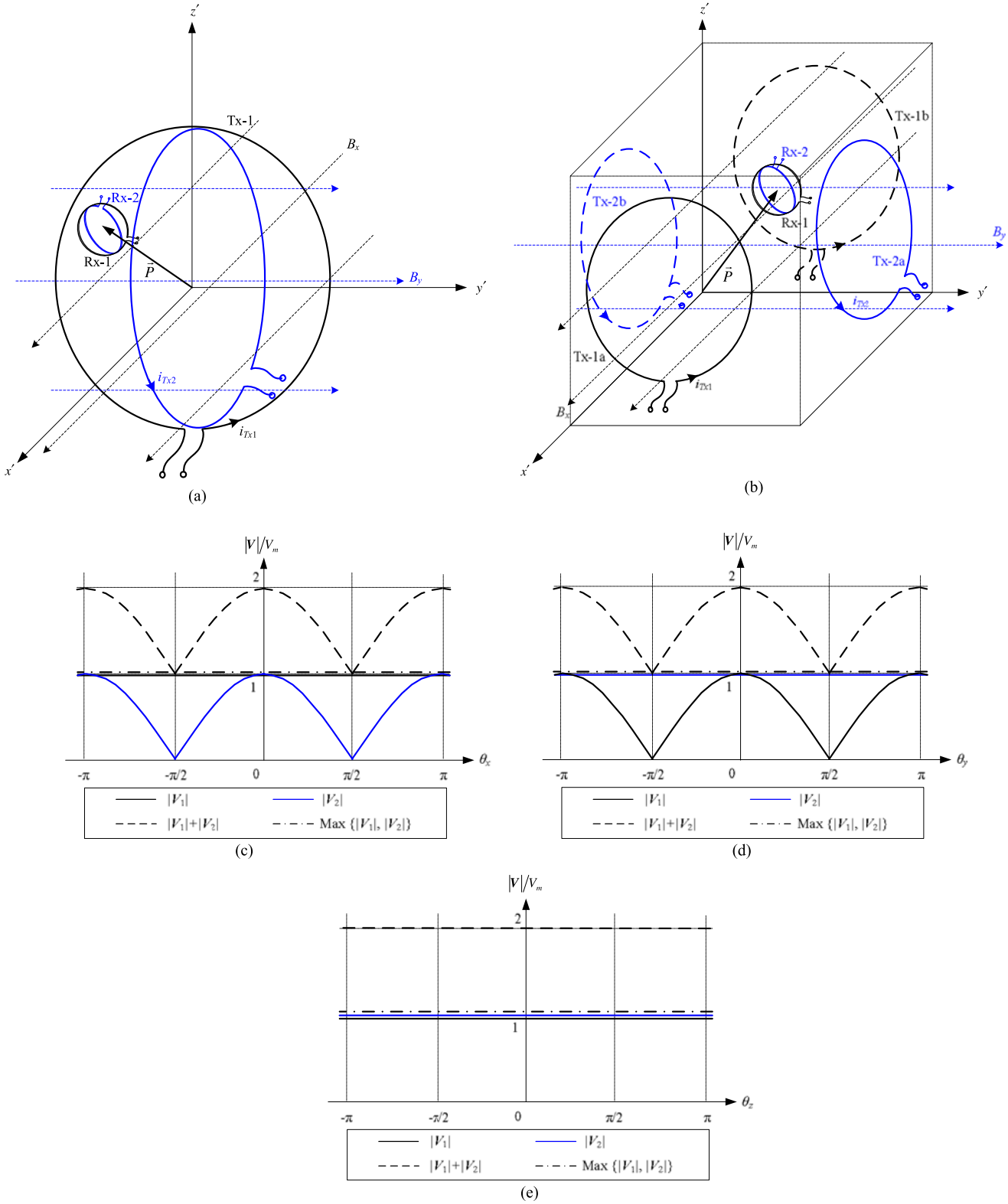

Fig. 8. 2Tx-2Rx coil configurations and their normalized values of induced Rx coil voltages when (m_T, m_R) is (2, 2). (a) 2Tx-2Rx coil configuration. (b) 2Tx-2Rx coil configuration, where a pair of loop coils facing each other is used for Tx. (c) Induced Rx coil voltages w.r.t. θ_x rotation. (d) Induced Rx coil voltages w.r.t. θ_y rotation. (e) Induced Rx coil voltages w.r.t. θ_z rotation.

TABLE II
POSSIBLE LOOP COIL COMBINATIONS FOR OMNIDIRECTIONAL POWERING

Numbers of orthogonal coils			Loop coil dimension	
m_T	m_R	$m_T + m_R$	n_{TL}	n_{RL}
1	3	4	2	3
2	2	4	3	3
2	3	5	3	3
3	1	4	3	2
3	2	5	3	3
3	3	6	3	3

Practically, three induced Rx coil voltages should be connected in series or in parallel to drive a single load R_L as shown in Fig. 6(c) and (d). For the convenience of analysis, it is assumed that the diode rectifiers are operating in a continuous-conduction mode with no loss. In addition, the reactance of each Rx coil is completely compensated by a series resonant capacitor C_s so that the induced coil voltages can be entirely applied to the diode rectifiers. A parallel resonant capacitor for each Rx coil may also be used for the compensation, though this is not shown here. For the series connection of Fig. 6(c), each Rx coil voltage is rectified and stacked at the dc stage for providing load voltage. On the other hand, the parallel connection of Fig. 6(d) automatically delivers the highest Rx coil voltage to the load. Then, the relationship between the Rx coil voltages and dc load voltage can be obtained for both the series and parallel connections as follows:

$$V_{Ls} \equiv V_{L1} + V_{L2} + V_{L3} = \frac{\pi}{2\sqrt{2}} \left(|\boldsymbol{V}_1| + |\boldsymbol{V}_2| + |\boldsymbol{V}_3|\right),$$

for the series connection (10a)

$$V_{Lp} = \frac{\pi}{2\sqrt{2}} \cdot \mathrm{Max}\left\{|\boldsymbol{V}_1|, |\boldsymbol{V}_2|, |\boldsymbol{V}_3|\right\},$$

for the parallel connection. (10b)

For an intuitive understanding of the influence of rotations, the magnitude portions of phasor voltages in (9) and (10) are depicted in Fig. 6(e)–(g). It is noteworthy that the normalized values of the both $|\boldsymbol{V}_1|+|\boldsymbol{V}_2|+|\boldsymbol{V}_3|$ and $\mathrm{Max}\left\{|\boldsymbol{V}_1|, |\boldsymbol{V}_2|, |\boldsymbol{V}_3|\right\}$ in Fig. 6(e)–(g) are always higher than$1/\sqrt{2}$ ($\sim$70.7%) over any rotation angles.

C. Triple Tx Coils and Single Rx Coils (3Tx-1Rx)

Another coil configuration offering the omnidirectional powering is the triple orthogonal Tx coils with a single Rx coil, where $(m_T, m_R) = (3, 1)$ [13]. Two possible coil configurations achieving $(m_T, m_R) = (3, 1)$ are illustrated in Fig. 7(a) and (b). For omnidirectional powering, the three Tx coil currents should be appropriately different from each other in order not to generate a constant magnetic field for a fixed direction. There are three possible modulation methods in general: 1) phase-domain modulation (PDM), 2) time-domain modulation (TDM), and 3) frequency-domain modulation (FDM). However, the TDM requires complex controls dealing

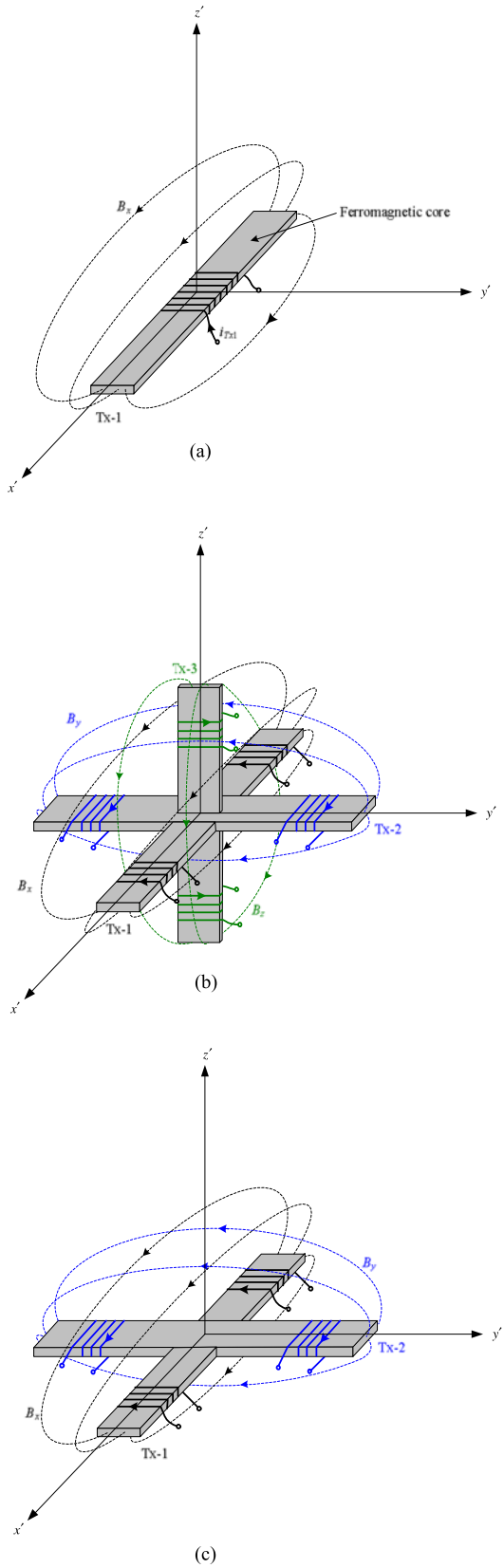

Fig. 9. Three dipole coil configurations corresponding to the Tx loop coils in Figs. 6–8. (a) Single dipole coil ($m_T = 1, n_{TD} = 1$). (b) Three orthogonal dipole coils ($m_T = 3, n_{TD} = 3$). (c) Two crossed dipole coils ($m_T = 2, n_{TD} = 2$).

TABLE III
POSSIBLE DIPOLE COIL COMBINATIONS FOR OMNIDIRECTIONAL POWERING

Numbers of orthogonal coils			Dipole coil dimension	
m_T	m_R	$m_T + m_R$	n_{TD}	n_{RD}
1	3	4	1	3
2	2	4	2	2
2	3	5	2	3
3	1	4	3	1
3	2	5	3	2
3	3	6	3	3

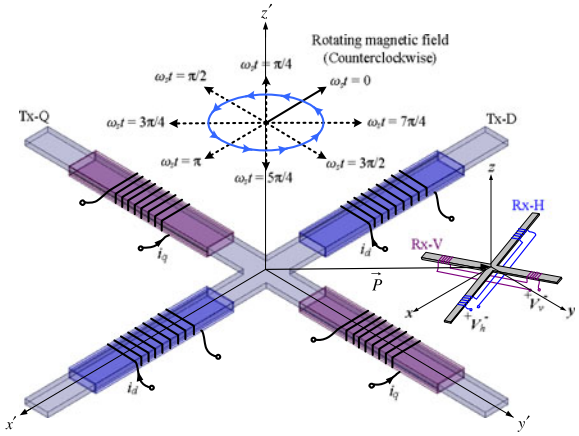

Fig. 10. DQ Rotating magnetic field generation of the proposed crossed dipole Tx coil.

with the dynamic responses of the Tx and Rx resonant circuits. The FDM is also not a viable solution, because it requires three resonant circuits of different frequency for an Rx. Hence, the PDM is mostly preferred, considering the simplicities of control and structure. Assuming that each Tx current has same magnitude with $2\pi/3$ phase difference from each other, the Rx coil voltage of (6) can be rewritten, when $B_x = B_y = B_z = B_0$, $\alpha_x = 0$, $\alpha_y = 2\pi/3$, and $\alpha_z = 4\pi/3$, as follows:

$$\boldsymbol{V}_1|_{\overrightarrow{n}=\overrightarrow{n}_1} = jV_m\left(\cos\theta_y\cos\theta_z\angle 0 + \cos\theta_y\sin\theta_z\angle 2\pi/3 - \sin\theta_y\angle 4\pi/3\right). \quad (11)$$

As shown in Fig. 7(c)–(e), the magnitude of phasor voltage in (11) can be rewritten as follows:

$$V_{1x} \equiv |\boldsymbol{V}_1||_{\overrightarrow{n}=\overrightarrow{n}_1,\theta_y=\theta_z=0} = V_m \quad (12a)$$

$$V_{1y} \equiv |\boldsymbol{V}_1||_{\overrightarrow{n}=\overrightarrow{n}_1,\theta_x=\theta_z=0} = V_m\left|\cos\theta_y\angle 0 - \sin\theta_y\angle 4\pi/3\right| = V_m\sqrt{1+0.5\sin 2\theta_y} \quad (12b)$$

$$V_{1z} \equiv |\boldsymbol{V}_1||_{\overrightarrow{n}=\overrightarrow{n}_1,\theta_x=\theta_y=0} = V_m\left|\cos\theta_z\angle 0 + \sin\theta_z\angle 2\pi/3\right| = V_m\sqrt{1-0.5\sin 2\theta_z}. \quad (12c)$$

Though there are voltage fluctuations w.r.t. θ_y and θ_z rotations, the lowest value of $|\boldsymbol{V}_1|$ is $1/\sqrt{2}$ ($\sim$70.7%) times of V_m over any rotation angles.

D. Double Tx Coils and Double Rx Coils (2Tx-2Rx)

Another candidate coil configuration of omnidirectional powering is the double Tx coils with double Rx coils, where both coils are composed of two orthogonal coils when each m_T and m_R is 2. As shown in Fig. 8(a) and (b), the Tx coils can be constituted with either a single set of two orthogonal coils or a dual set of two orthogonal coils, respectively. In a similar fashion to the 3Tx-1Rx configuration, the PDM is preferred to drive each Tx current.

Assuming that each Tx current has same magnitude with $\pi/2$ phase difference from each other, the Rx coil voltage can be rewritten from (6) and (8), when $B_x = B_y = B_0$, $B_z = 0$, $\alpha_x = 0$, and $\alpha_y = \pi/2$, as follows:

$$\boldsymbol{V}_1|_{\overrightarrow{n}=\overrightarrow{n}_1} = V_m\cos\theta_y\left(-\sin\theta_z + j\cos\theta_z\right) \quad (13a)$$

$$\boldsymbol{V}_2|_{\overrightarrow{n}=\overrightarrow{n}_2} = V_m\left(-\sin\theta_x\sin\theta_y\sin\theta_z - \cos\theta_x\cos\theta_z + j\sin\theta_x\sin\theta_y\cos\theta_z - j\cos\theta_x\sin\theta_z\right). \quad (13b)$$

As shown in Fig. 8(c)–(e), the magnitude of phasor voltage in (13) can be rewritten as follows:

$$V_{1x} \equiv |\boldsymbol{V}_1||_{\overrightarrow{n}=\overrightarrow{n}_1,\theta_y=\theta_z=0} = V_m \quad (14a)$$

$$V_{1y} \equiv |\boldsymbol{V}_1||_{\overrightarrow{n}=\overrightarrow{n}_1,\theta_x=\theta_z=0} = \omega_s N_{\mathrm{Rx}} A_{\mathrm{Rx}} B_0\left|\cos\theta_y\right| = V_m\left|\cos\theta_y\right| \quad (14b)$$

$$V_{1z} \equiv |\boldsymbol{V}_1||_{\overrightarrow{n}=\overrightarrow{n}_1,\theta_x=\theta_y=0} = \omega_s N_{\mathrm{Rx}} A_{\mathrm{Rx}} B_0\left|\cos\theta_z + j\sin\theta_z\right| = V_m \quad (14c)$$

$$V_{2x} \equiv |\boldsymbol{V}_2||_{\overrightarrow{n}=\overrightarrow{n}_2,\theta_y=\theta_z=0} = \omega_s N_{\mathrm{Rx}} A_{\mathrm{Rx}} B_0\left|j\cos\theta_x\right| = V_m\left|\cos\theta_x\right| \quad (14d)$$

$$V_{2y} \equiv |\boldsymbol{V}_2||_{\overrightarrow{n}=\overrightarrow{n}_2,\theta_x=\theta_z=0} = V_m \quad (14e)$$

$$V_{2z} \equiv |\boldsymbol{V}_2||_{\overrightarrow{n}=\overrightarrow{n}_2,\theta_x=\theta_y=0} = \omega_s N_{\mathrm{Rx}} A_{\mathrm{Rx}} B_0\left|-\sin\theta_z + j\cos\theta_z\right| = V_m. \quad (14f)$$

Under the same assumptions in the 3Tx-1Rx configuration analysis, the Rx coil voltages and dc load voltage can be obtained for both the series and parallel connections as follows:

$$V_{Ls} \equiv V_{L1} + V_{L2} = \frac{\pi}{2\sqrt{2}}\left(|\boldsymbol{V}_1| + |\boldsymbol{V}_2|\right), \quad \text{for the series connection} \quad (15a)$$

$$V_{Lp} = \frac{\pi}{2\sqrt{2}}\cdot\mathrm{Max}\left\{|\boldsymbol{V}_1|, |\boldsymbol{V}_2|\right\}, \quad \text{for the parallel connection.} \quad (15b)$$

As identified from (15) and Fig. 8, the dc load voltages are always higher than 0.5 times of their maximum values over any rotation angles. Note that the series connection provides a fluctuated but higher dc load voltage than that of the parallel connection, whereas the parallel connection provides a relatively constant but lower dc load voltage.

Remark that the voltage profiles shown in Figs. 6–8 are specific cases of only one rotation among θ_x, θ_y, and θ_z rotations.

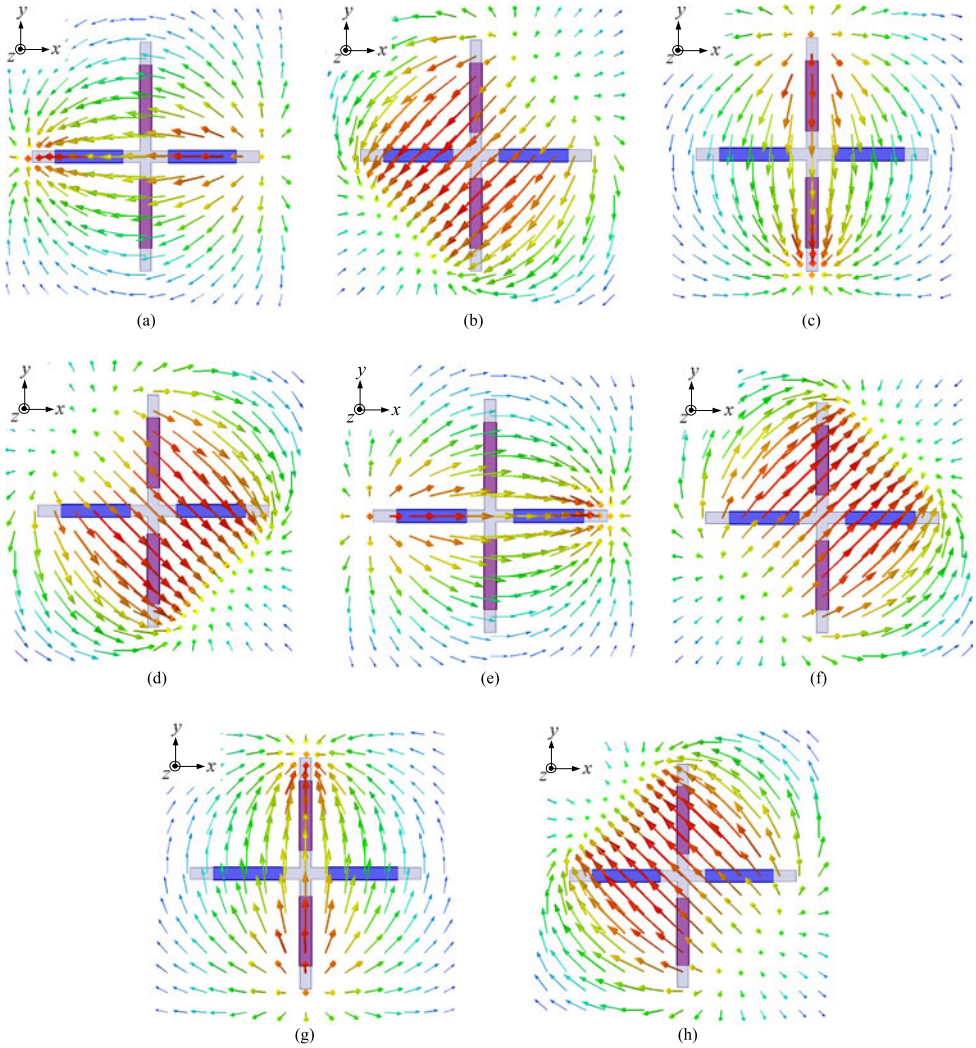

Fig. 11. FEM simulation of the proposed Tx coil with two orthogonal currents i_d and i_q. (a) $\omega_s t = 0$. (b) $\omega_s t = \pi/4$. (c) $\omega_s < t = \pi/2$. (d) $\omega_s t = 3\pi/4$. (e) $\omega_s t = p$. (f) $\omega_s t = 5\pi/4$. (g) $\omega_s t = 3\pi/2$. (h) $\omega_s t = 7\pi/4$.

In practice, the rotation of an Rx could be arbitrary and θ_x, θ_y, and θ_z are not correlated each other in general so they may be all nonzeros.

E. Omnidirectional Powering Conditions in IPT

Based on the analyses, results in the previous sections, the necessary condition of the omnidirectional powering in the IPT can be derived as follows:

$$m_T + m_R \geq 4 \tag{16}$$

where each Tx current is not correlated when m_T is higher than 1. Note that the aforementioned cases of 1Tx-3Rx, 3Tx-1Rx, and 2Tx-2Rx.

Based on the above discussions so far, six possible loop coil combinations for omnidirectional powering are listed in Table II, where the physical dimensions of Tx and Rx coils are defined as n_{TL} and n_{RL}, respectively. Note that, as is found from Figs. 6–8, the volumetric coil structure is inevitable for at least one of Tx and Rx coils with the loop coils, which is one of the motivations to propose the crossed dipole coil structure in the subsequent section.

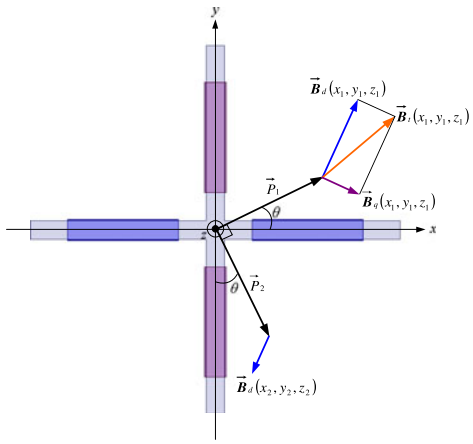

Fig. 12. Magnetic flux densities generated from Tx-D (x-axis) and Tx-Q (y-axis) coils.

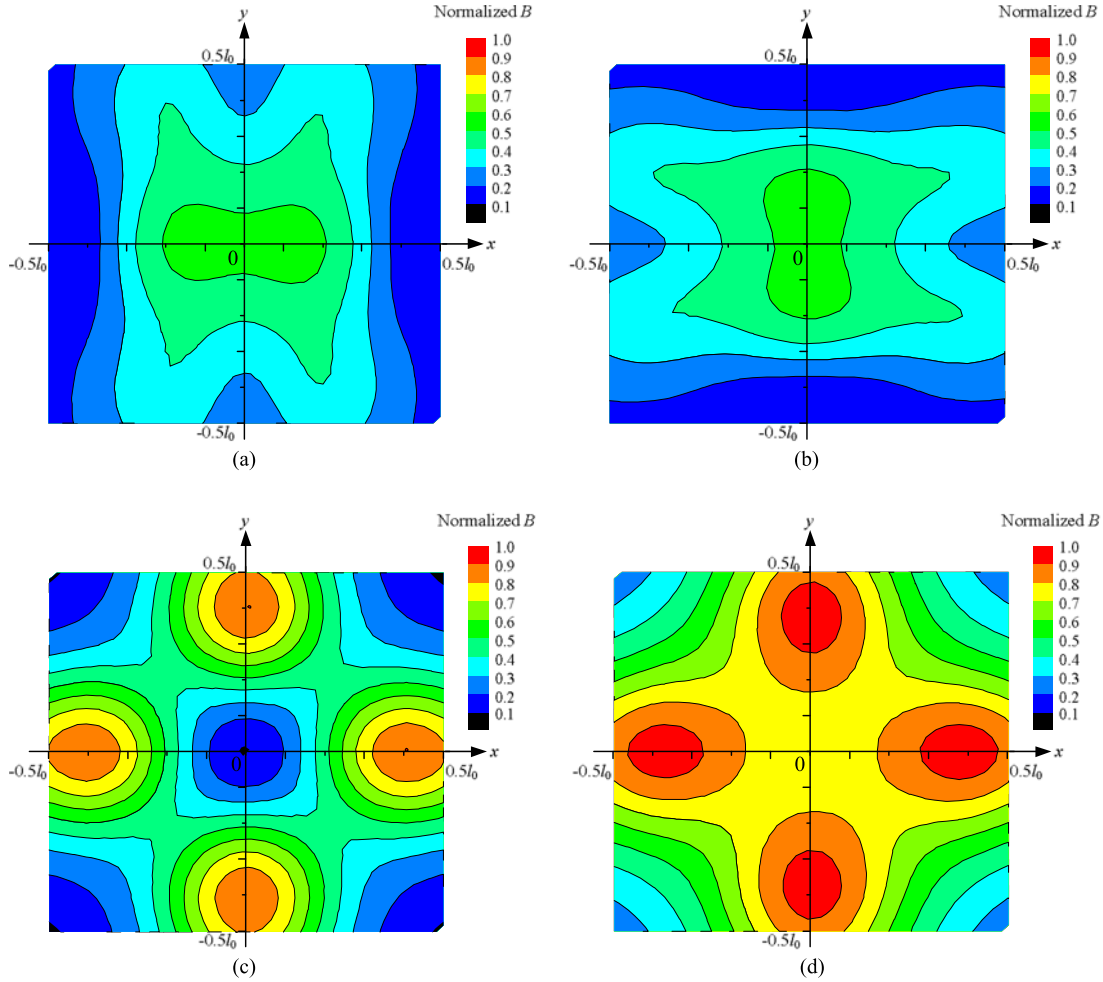

Fig. 13. Synthesized magnetic flux density at $z = 0.25l_0$ using (22), based on the FEM simulation results. (a) $|B_{dx} + jB_{qx}|$. (b) $|B_{dy} + jB_{qy}|$. (c) $|B_{dz} + jB_{qz}|B_t$. (d) B_t.

IV. Analysis and Design of the Proposed Crossed Dipole Coils

A. Omnidirectional WPTs by Dipole Coils

In order to reduce the physical dimension of omnidirectional powering coils, the dipole coil structure [19], [20] is adopted instead of the loop coils as shown in Fig. 9. Using ferromagnetic core, such as ferrite, amorphous, and silicon steel in the dipole coils, the physical dimensions of Tx and Rx are reduced from volume to plane and from plane to line compared to the loop coils. Thus, the coil structures for omnidirectional powering are not necessarily volumetric when the plane-type crossed dipole coils in Fig. 9(c) are used for both Tx and Rx coils to accomplish (m_T, m_R) of (2, 2).

Unlike the loop coil configurations, the theoretical derivation of the induced Rx coil voltage for a given Tx coil structure and current is not straightforward because of the complicated magnetic field distorted by the ferromagnetic core. Therefore, a simulation-based coil design is inevitably adopted in this paper.

In a similar fashion to the previous section, several possible combinations for omnidirectional powering are listed in Table III, where the physical dimensions of Tx and Rx coils are defined as n_{TD} and n_{RD}, respectively. Though not shown here, the combinations of Tx loop coils and Rx dipole coils, and vice versa, are also possible to implement the 6 DoF IPT.

B. Simulation-Based Design of the Proposed Crossed Dipole Tx and Rx Coils

For most practical applications, neither Tx nor Rx coils should be in volumetric configuration. Excluding the cases of either $n_{TD} = 3$ or $n_{RD} = 3$ from Table III, the 2Tx-2Rx configuration is the only viable case where both Tx and Rx coils are of plane type. The synchronized DQ inverter is introduced in this paper to provide two orthogonal phased Tx currents as shown in Fig. 3. The switching angular frequency of the DQ inverter ω_s is a little higher than the resonant frequency determined by the Tx coils and compensating capacitors C_D and C_Q so that the inverter switches may operate at zero voltage switching condition [41]–[44]. By using the Rx coil of identical shape but smaller size than the Tx coil, both free-positioning and omnidirectional powering are achieved.

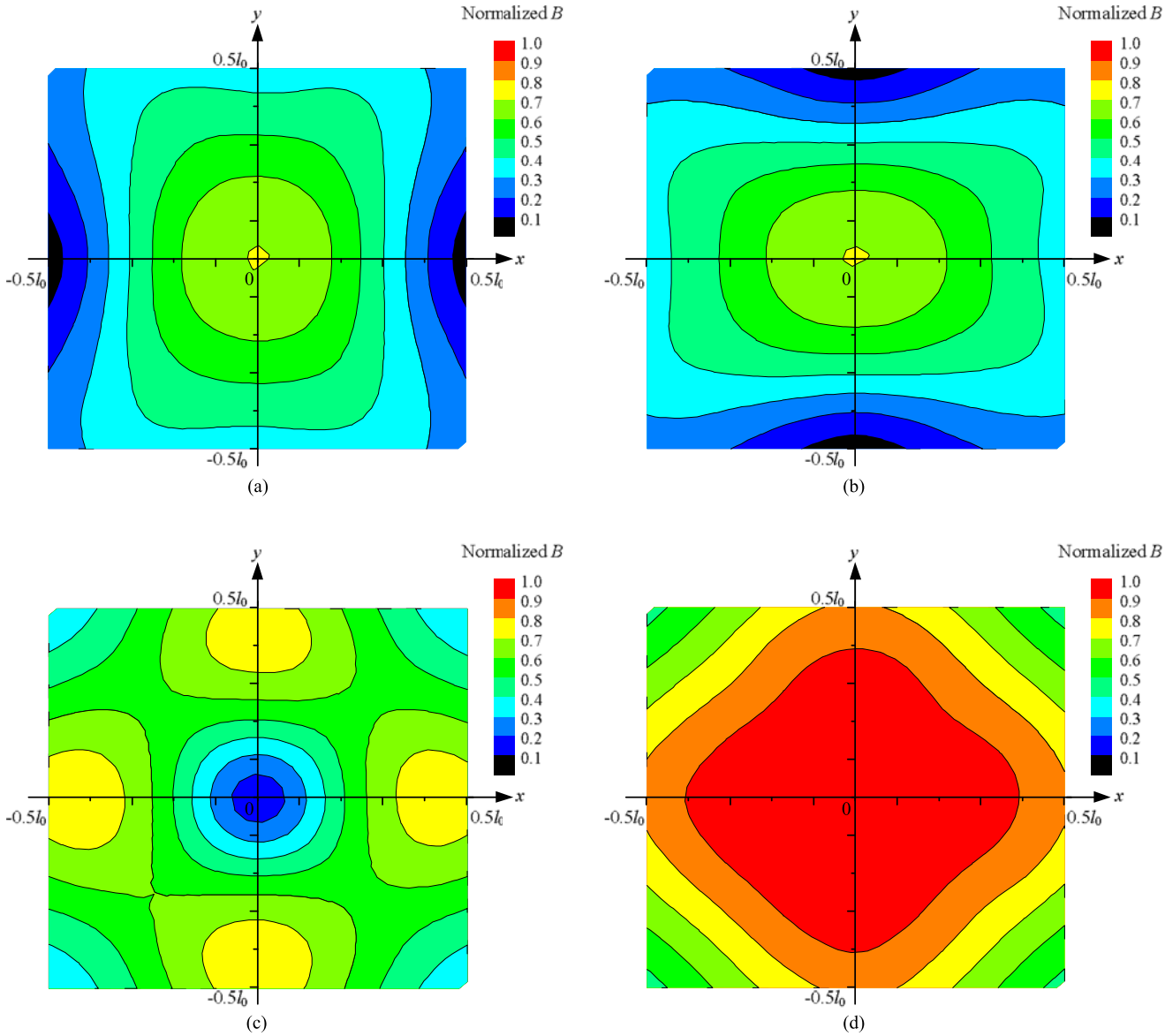

Fig. 14. Synthesized magnetic flux density at $z = 0.5l_0$ using (22), based on the FEM simulation results. (a) $|B_{dx} + jB_{qx}|$. (b) $|B_{dy} + jB_{qy}|$. (c) $|B_{dz} + jB_{qz}|$. (d) B_t.

As shown in Fig. 10, the rotating magnetic field in the steady state is formed by two orthogonal dipole coils of Tx-D and Tx-Q having identical magnitude of currents $\boldsymbol{I_d}$ and $\boldsymbol{I_q}$, respectively, as follows:

$$\boldsymbol{I}_d \equiv I_d \angle 0 \tag{17a}$$

$$\boldsymbol{I}_q \equiv I_d \angle \pi/2 = j\boldsymbol{I}_d. \tag{17b}$$

Both magnetic flux density vectors $\overrightarrow{\boldsymbol{B}}_d$ and $\overrightarrow{\boldsymbol{B}}_q$, which are generated by the two orthogonal dipole Tx currents in (17), can be described of phasor form as follows:

$$\begin{aligned}\overrightarrow{\boldsymbol{B}}_d &\equiv (\boldsymbol{B}_{dx}, \boldsymbol{B}_{dy}, \boldsymbol{B}_{dz}) \\ &= (B_{dx}\angle 0, B_{dy}\angle 0, B_{dz}\angle 0) \\ &= (B_{dx}, B_{dy}, B_{dz})\end{aligned} \tag{18a}$$

$$\begin{aligned}\overrightarrow{\boldsymbol{B}}_q &\equiv (\boldsymbol{B}_{qx}, \boldsymbol{B}_{qy}, \boldsymbol{B}_{qz}) \\ &= (B_{qx}\angle \pi/2, B_{qy}\angle \pi/2, B_{qz}\angle \pi/2) \\ &= (jB_{qx}, jB_{qy}, jB_{qz}).\end{aligned} \tag{18b}$$

Note that the phasor of $\overrightarrow{\boldsymbol{B}}_q$ is $\pi/2$ ahead of $\overrightarrow{\boldsymbol{B}}_d$; however, the magnitude of $\overrightarrow{\boldsymbol{B}}_q$ is irrelevant to $\overrightarrow{\boldsymbol{B}}_d$ although the magnitudes of two currents $\boldsymbol{I}_{\mathrm{d}}$ and $\boldsymbol{I}_{\mathrm{q}}$ are identical.

Then, the polarities of the summed magnetic field $\overrightarrow{\boldsymbol{B}}_t$ on the *xy* plane rotate around the coils as shown in Fig. 11, where the finite-element method (FEM) simulations of magnetic field line by ANSYS Maxwell v15 are shown for a switching period. Omnidirectional powering can be obtained by the proposed crossed dipole Tx and Rx coils of plane type as a result of this rotating magnetic field.

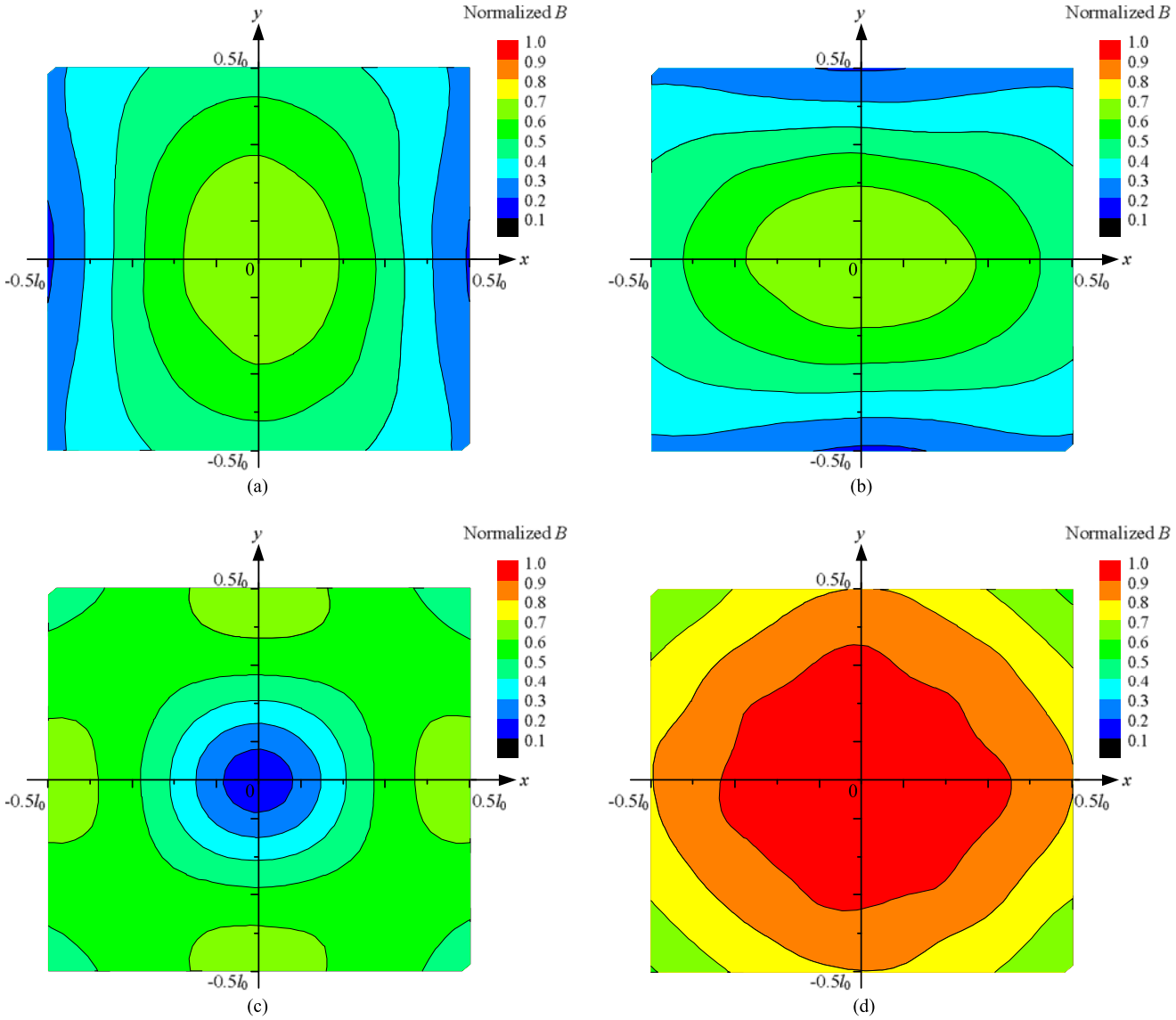

Fig. 15. Synthesized magnetic flux density at $z = 0.75l_0$ using (22), based on the FEM simulation results. (a) $|B_{dx} + jB_{qx}|$. (b) $|B_{dy} + jB_{qy}|$. (c) $|B_{dz} + jB_{qz}|$. (d) B_t.

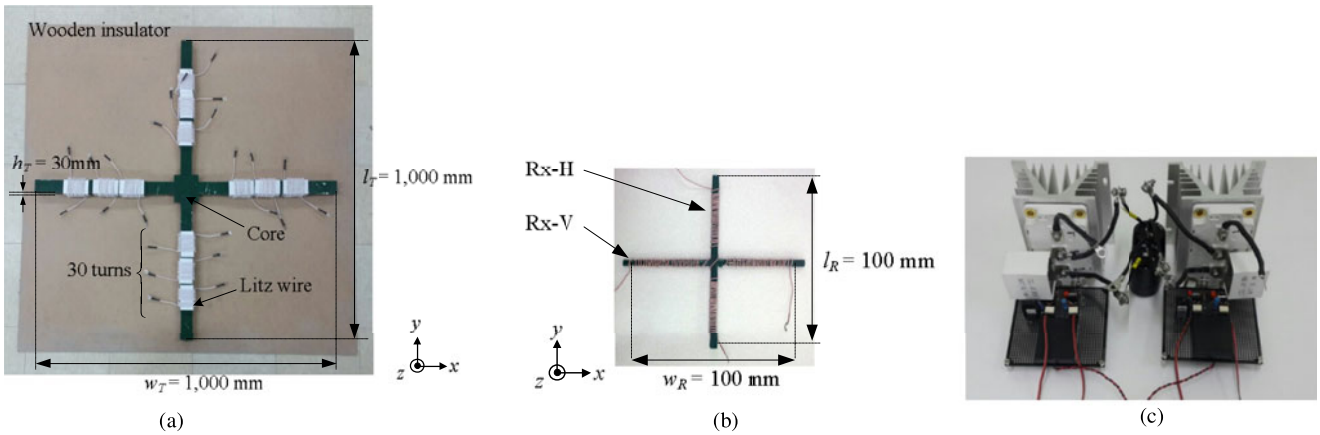

Fig. 16. Fabricated prototypes. (a) Tx coil with an aluminum plate. (b) Rx coil having h_R of 1 mm. (c) DQ inverter.

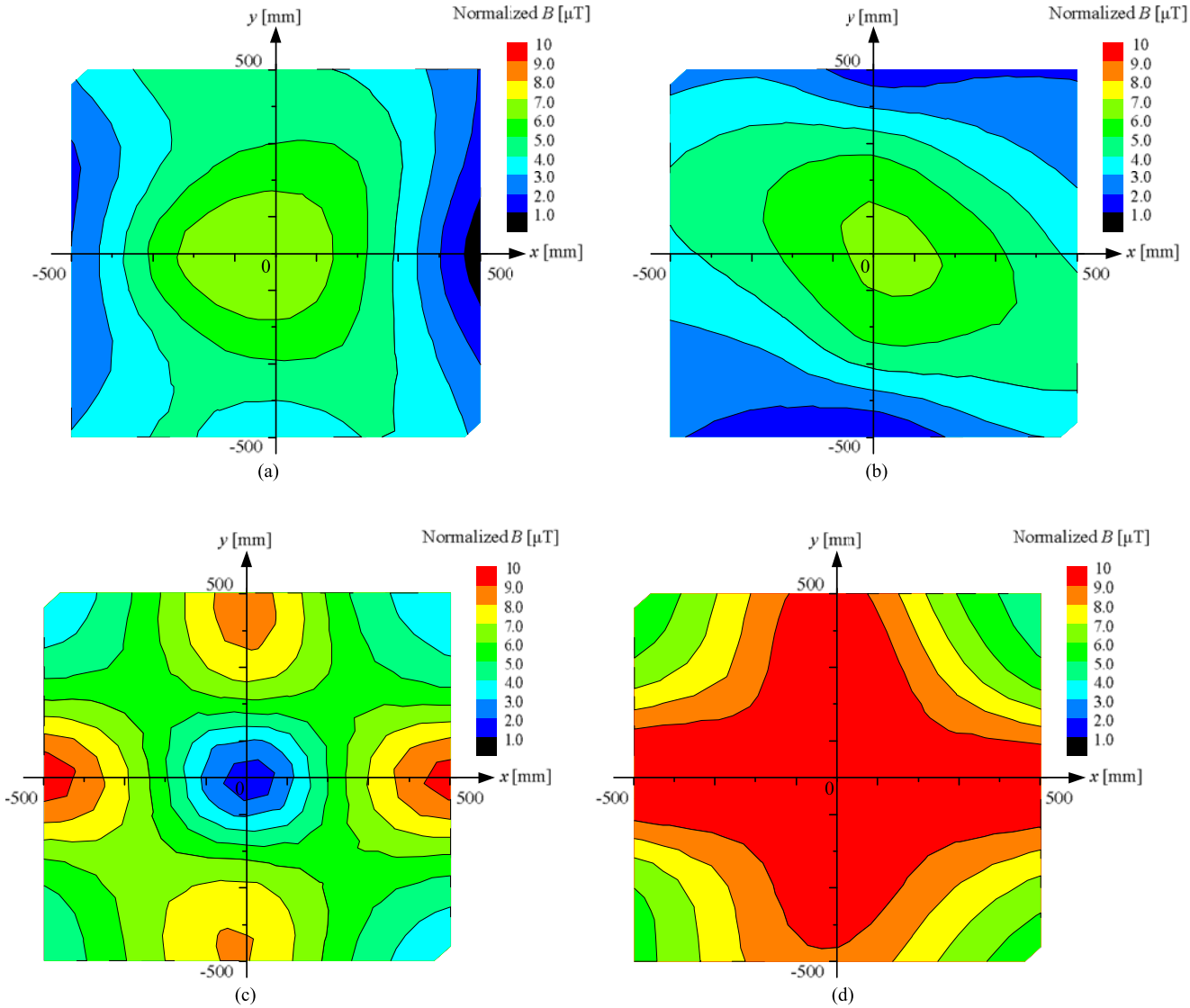

Fig. 17. Measured magnetic flux density at $z = l_0/2 = 500$ mm. (a) x-direction magnetic flux density $|B_{dx} + jB_{qx}|$. (b) y-direction magnetic flux density $|B_{dy} + jB_{qy}|$. (c) z-direction magnetic flux density $|B_{dz} + jB_{qz}|$. (d) Summed magnetic flux density $|B_t|$.

From (18), $\overrightarrow{\boldsymbol{B}}_t$ can be derived as follows:

$$\begin{aligned}\overrightarrow{\boldsymbol{B}}_t &\equiv \overrightarrow{\boldsymbol{B}}_d + \overrightarrow{\boldsymbol{B}}_q = (\boldsymbol{B}_{dx} + \boldsymbol{B}_{qx}, \boldsymbol{B}_{dy} + \boldsymbol{B}_{qy}, \boldsymbol{B}_{dz} + \boldsymbol{B}_{qz}) \\ &= (B_{dx} + jB_{qx}, B_{dy} + jB_{qy}, B_{dz} + jB_{qz}) . \end{aligned} \tag{19}$$

Then, the magnitude of (19) can be determined as follows:

$$\begin{aligned} B_t &\equiv \left|\overrightarrow{\boldsymbol{B}}_t\right| = \left|\overrightarrow{\boldsymbol{B}}_d + \overrightarrow{\boldsymbol{B}}_q\right| \\ &= \sqrt{\left|\boldsymbol{B}_{dx} + \boldsymbol{B}_{qx}\right|^2 + \left|\boldsymbol{B}_{dy} + \boldsymbol{B}_{qy}\right|^2 + \left|\boldsymbol{B}_{dz} + \boldsymbol{B}_{qz}\right|^2} \\ &= \sqrt{\left|B_{dx} + jB_{qx}\right|^2 + \left|B_{dy} + jB_{qy}\right|^2 + \left|B_{dz} + jB_{qz}\right|^2} \\ &= \sqrt{B_{dx}^2 + B_{qx}^2 + B_{dy}^2 + B_{qy}^2 + B_{dz}^2 + B_{qz}^2} \\ &= \sqrt{B_{dx}^2 + B_{dy}^2 + B_{dz}^2 + B_{qx}^2 + B_{qy}^2 + B_{qz}^2} \\ &= \sqrt{\left|\overrightarrow{\boldsymbol{B}}_d\right|^2 + \left|\overrightarrow{\boldsymbol{B}}_q\right|^2} \\ &= \sqrt{B_d^2 + B_q^2} B_d \equiv \left|\overrightarrow{\boldsymbol{B}}_d\right|, B_q \equiv \left|\overrightarrow{\boldsymbol{B}}_q\right| . \end{aligned} \tag{20}$$

As identified from (20), the magnitude of the total magnetic field density B_t is determined only by B_d and B_q, and is irrelevant to the vector direction. As shown in Fig. 12, B_q can be found from B_d, considering the symmetric structures of the Tx coils and identical magnitude of DQ currents as follows:

$$\begin{aligned} &B_q(x_1, y_1, z_1) = \left|\overrightarrow{\boldsymbol{B}}_q(x_1, y_1, z_1)\right| = \left|\overrightarrow{\boldsymbol{B}}_d(x_2, y_2, z_2)\right| \\ &= B_d(y_1, -x_1, z_1) \\ &\therefore B_q(x, y, z) = B_d(y, -x, z), \text{ for arbitrary } x, y, z. \end{aligned} \tag{21}$$

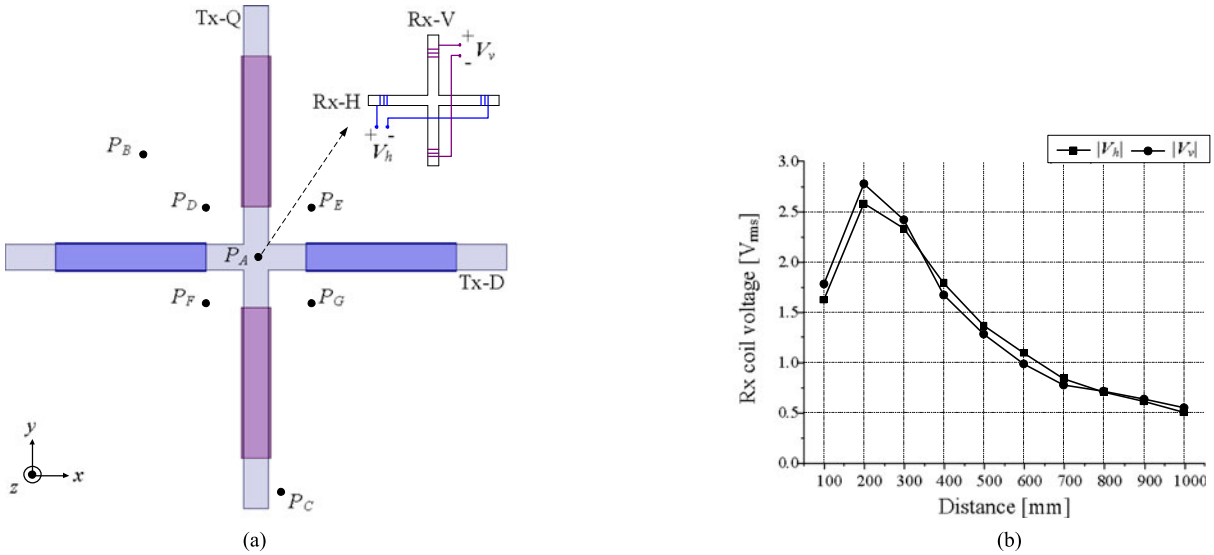

Fig. 18. Experimental conditions and Rx coil voltages along z-axis. (a) Seven measuring points. (b) Rx coil voltages w.r.t the z-axis distance at P_A.

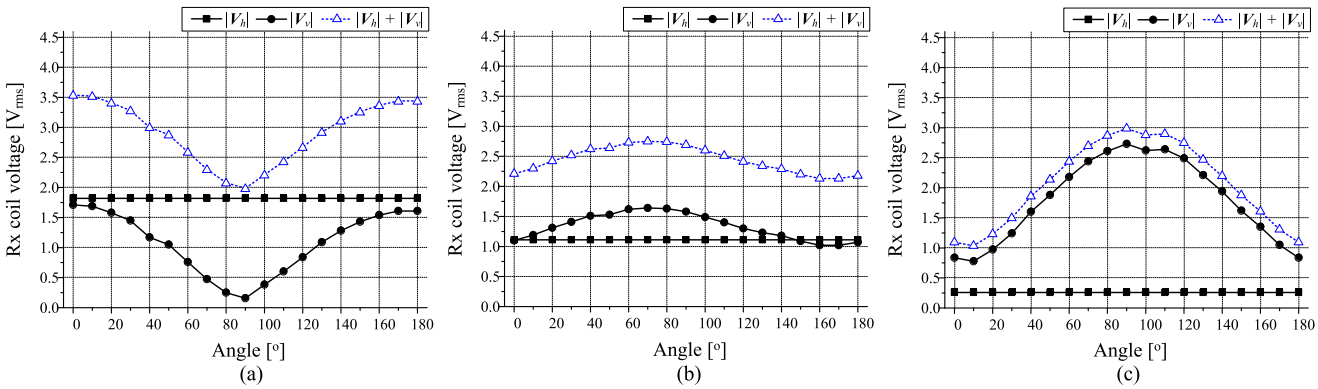

Fig. 19. Measured Rx coil voltages for pitch rotation. (a) P_A, (b) P_B, and (c) P_C.

In (21), the fact that the magnitude of magnetic flux density from a Tx-Q at a position $\overrightarrow{P}_1$ should be the same as that from a Tx-D at the same relative position $\overrightarrow{P}_2$is used. Applying (21) to (20) results in the following formula:

$$B_t(x,y,z) = \sqrt{B_d^2(x,y,z) + B_q^2(x,y,z)} = \sqrt{B_d^2(x,y,z) + B_d^2(y,-x,z)}. \quad (22)$$

As identified from (22), B_t can be completely determined by B_d, which can be found from simulation or experiment. Therefore, the total rms value of magnetic flux density can be simply found from a single axis dc analysis instead of DQ axis ac time-domain analysis, which is time consuming and does not give us the useful rms value as shown in Fig. 11.

Using (22) and the FEM simulation result for the magnetic field density from a Tx-D coil, the effective powering area for Rx is evaluated for $z = 0.25l_0$, $z = 0.5l_0$, and $z = 0.75l_0$ over the xy plane as shown in Figs. 13–15, where l_0 is the length of a Tx coil. An aluminum plate is displaced at the bottom of the Tx to block the magnetic field. The magnitudes of the magnetic field density in Figs. 13–15 are normalized with respect to their maximum values at each height. The x- and y-directional magnetic field densities reach their maximum at the center of the Tx coils and decrease away the center on the xy plane, whereas the z-directional magnetic field density reaches its maximum at both ends of each Tx coil. Therefore, a relatively even powering area can be achieved from the summed magnetic field, which is the result of averaging over three-directional magnetic flux density.

V. Experimental Verifications

A. Prototype Fabrication of 1-m^2-Sized Crossed Dipole Tx Coil

The design principle of the previous section has been applied to the prototype Tx and Rx coils operating at 280 kHz, where the Tx coil size is $l_T = w_T = 1000$ mm, and $h_T = 30$ mm and the Rx coil size is $l_R = w_R = 100$ mm, and $h_R = 1$ mm as shown in Fig. 16(a) and (b). The selection of design parameters in this paper is just for demonstration of the proposed concept

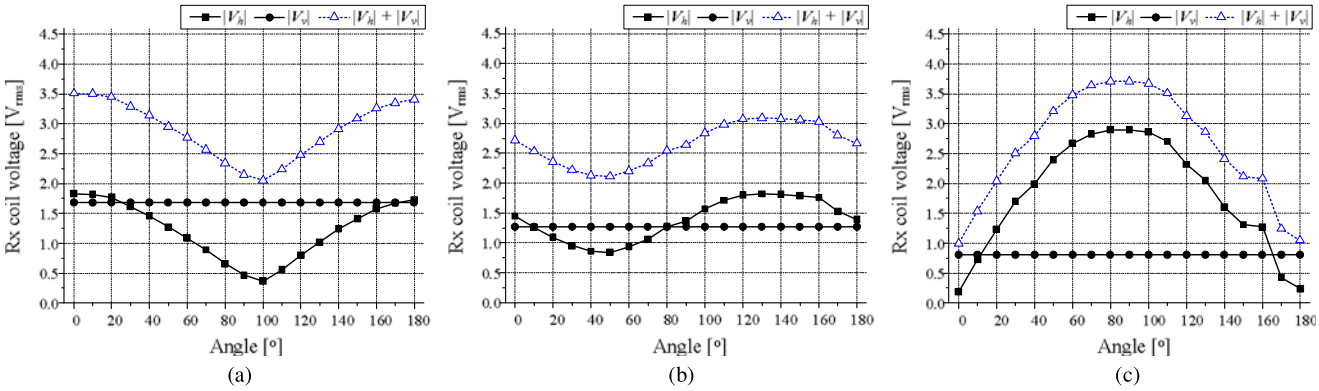

Fig. 20. Measured Rx coil voltages for roll rotation. (a) P_A, (b) P_B, and (c) P_C.

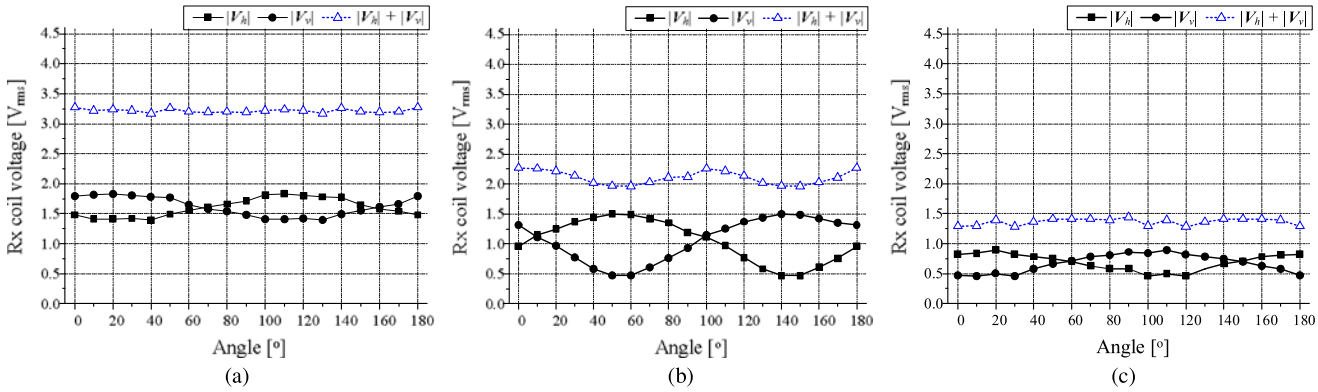

Fig. 21. Measured Rx coil voltages for yaw rotation. (a) P_A, (b) P_B, and (c) P_C.

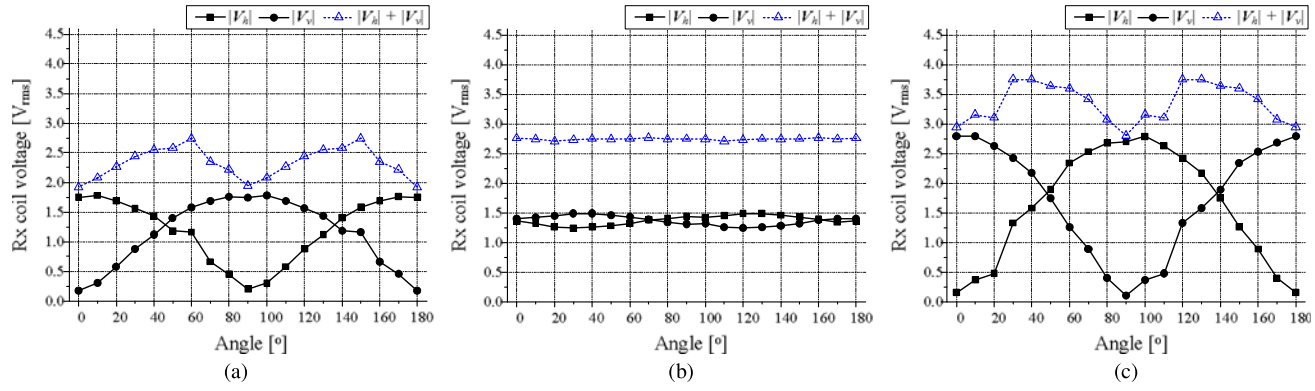

Fig. 22. Measured Rx coil voltages for 90°- pitched roll rotation. (a) P_A, (b) P_B, and (c) P_C.

and not intended for optimization of cost, mass, volume, and efficiency. For practical applications, the thicknesses of Tx and Rx coils h_T and h_R were selected as small as possible. The plane-shaped Mn–Zn ferrite cores having high permeability of 2000 were assembled for the Tx coil, where the unit size of the ferrite core is 100 mm $\times$ 50 mm $\times$ 10 mm. An experimental DQ inverter having the operating frequency of 280 kHz, which meets the guideline of PMA, was also fabricated to drive Tx currents with an efficiency of 97% as shown in Fig. 16(c). Litz wires having a total diameter of 1.8 mm were selected for the Tx coil, where the ampere-turn of each Tx coil was 120 AT and the number of turns was 60. An aluminum plate of 1.44 m^2 area and 2 mm thickness with a wooden insulator of 3 mm was displaced under the Tx coil. The total power loss including the

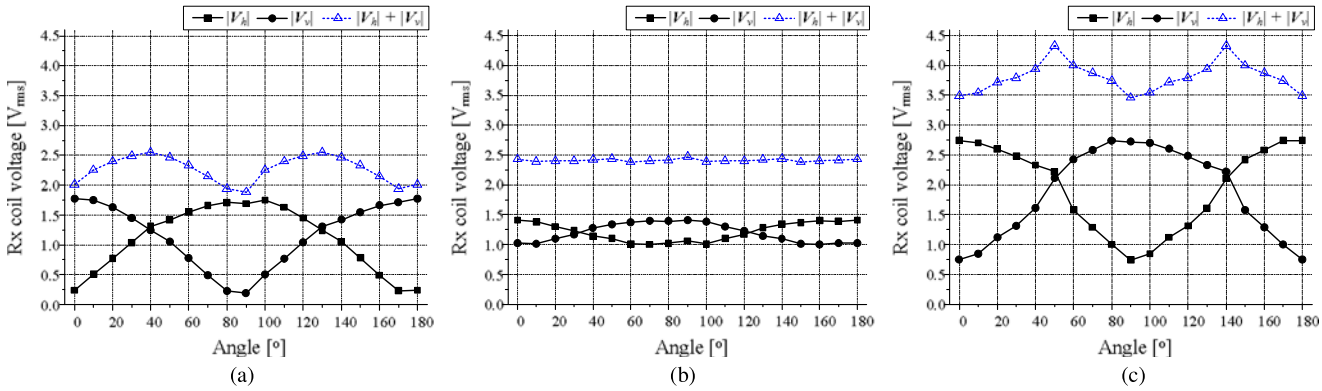

Fig. 23. Measured Rx coil voltages for 90°- rolled pitch rotation. (a) P_A, (b) P_B, and (c) P_C.

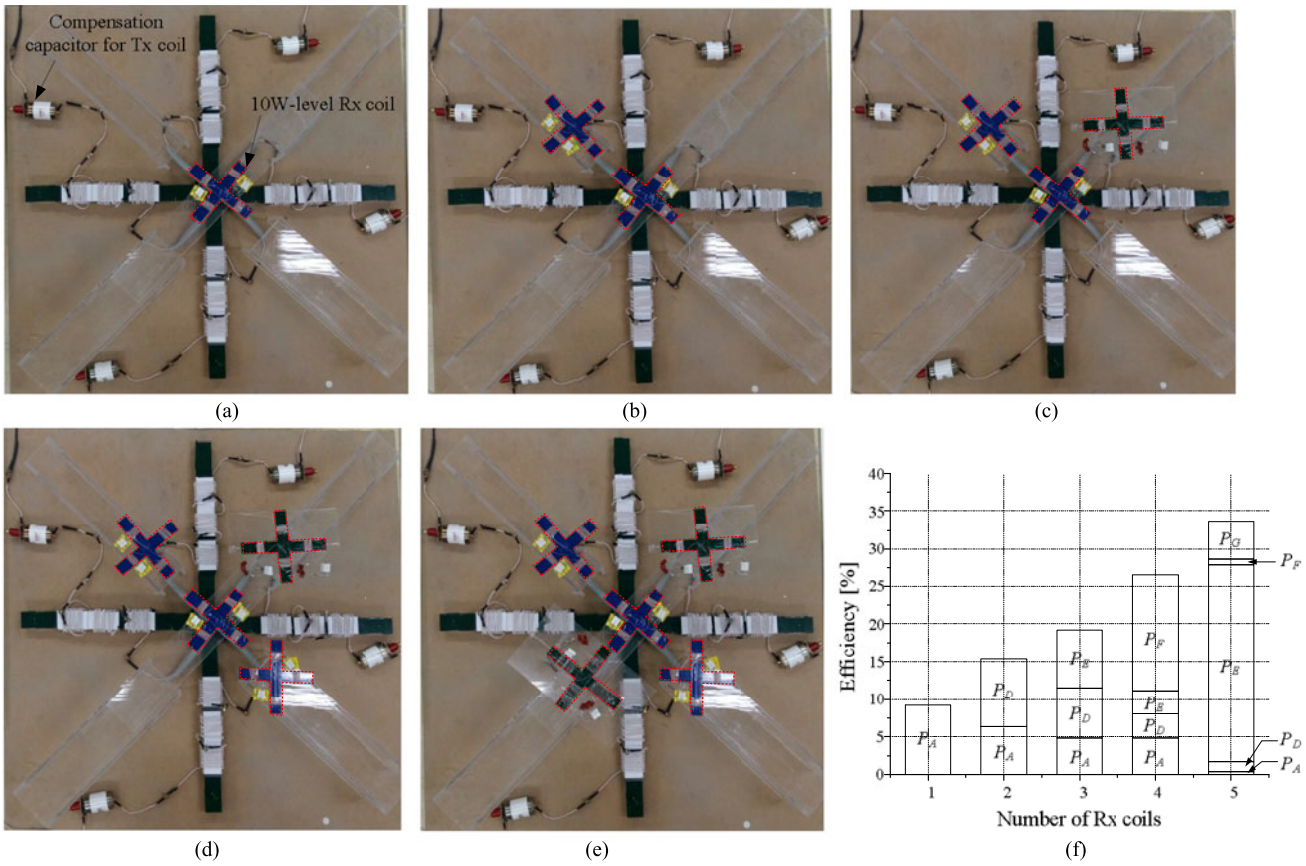

Fig. 24. Efficiency measurements with 10-W-level Rx coils. (a) One Rx coil at P_A. (b) Two Rx coils at P_A and P_D. (c) Three Rx coils at P_A, P_D, and P_E. (d) Four Rx coils at P_A, P_D, P_E, and P_F. (e) Five Rx coils at P_A, P_D, P_E, P_F, and P_G. (f) Efficiencies versus the number of Rx coils.

DQ inverter was 185 W, where the core loss was relatively high compared to the Litz wire and high-frequency applicable film capacitors, which have negligible conduction losses.

The experimental results are illustrated in Fig. 17, where B_t is determined as in (21). The measured effective powering area agreed fairly well with the simulation results in Fig. 14, where the maximum B_t was measured as 10.4 μT at $z = l_0/2 = 500$ mm.

B. Verification of Omnidirectional Powering

Fig. 18(a) shows seven measuring positions, which were arbitrarily selected to verify the free-positioning and omnidirectional powering characteristics. Both horizontal and vertical Rx coil voltages of $|\boldsymbol{V}_\mathrm{h}|$ and $|\boldsymbol{V}_\mathrm{v}|$ were measured along the z-axis from $z = 100$ to 1000 mm at point P_A as shown in Fig. 18(b). The slightly lower coil voltage at $z = 100$ mm compared to that at z = 200 mm was due to the low x- and y-directional magnetic flux densities close to the center of dipole coils. The Rx coil voltages with respect to five possible rotations, which are pitch, roll, yaw, 90°-pitched roll, and 90°-rolled pitch, were measured at three different positions of P_A, P_B, and P_C at $z = 500$ mm as shown in Figs. 19–23. As shown in Fig. 18(a), before any rotating of the Rx coils, the Rx-H and Rx-V are in

parallel with the *x*-axis and *y*-axis, respectively. The 90°-pitched roll denotes the roll rotation of the Rx coils after the Rx coils are 90° pitch rotated. Likewise, 90°-rolled pitch denotes the pitch rotation of the Rx coils after the Rx coils are 90° roll rotated. The series connected voltage $|\boldsymbol{V}_{\rm h}| + |\boldsymbol{V}_{\rm v}|$ ranged from 1.0 to 3.8 V over wide rotations for the selected points. Therefore, both free-positioning and omnidirectional powering were verified with the fabricated Tx and Rx coils.

C. Efficiency Measurements with 10-W-Level Rx Coils

The efficiency of the prototype Tx and Rx coils including the DQ inverter was measured for a few Rx coils as shown in Fig. 24. For the efficiency measurements, 10-W-level Rx coils having $l_R = 200$ mm, $w_R = 200$ mm, and $h_R = 5$ mm were located at P_A, P_D, P_E, P_F, and P_G as shown in Fig. 24(a)–(e). The measured efficiency increased as the number of Rx coils increased, where the maximum efficiency was 33.6% when the input power of the DQ inverter was fixed to 100 W for the case of five 10-W-level Rx coils at $z = 200$ mm. Due to the cross coupling between adjacent Rx coils having fixed compensation circuits, the output powers of each Rx coil were changed as the number of Rx coils increased.

VI. Conclusion

The crossed dipole Tx and Rx coils having 6 DoF in mobile IPTs with a DQ rotating magnetic field have been verified both by simulations and experiments throughout this paper. A general classification of various IPTs in terms of DoF was first presented, and a thorough analysis of loop coil configurations for omnidirectional powering was also provided so that the minimum physical dimensions for ubiquitous powering can be found for both Tx and Rx coils. Throughout this general survey on omnidirectional powering, the proposed crossed dipole Tx and Rx coils was found to be the only viable configuration that enables us both plane-type Tx and Rx coils. By virtue of a rotating magnetic field, both free-positioning and omnidirectional powering were guaranteed over a wide area of the Tx coil. The maximum efficiency of the prototype including the DQ inverter was measured as 33.6% when the input power was fixed to 100 W. Due to its plane geometry and the wide powering area, the proposed crossed dipole coil can be applied to mobile devices as well as IoT, where less dependence on battery will be required. An optimized design of the crossed dipole coil is left for future work.

References

[1] M. Kline, I. Izyumin, B. Boser, and S. Sanders, "Capacitive power transfer for contactless charging," in *Proc. IEEE Energy Convers. Congr. Expo.*, 2011, pp. 1398–1404.

[2] B. Choi, D. Nguyen, S. Yoo, J. Kim, and Chun T. Rim, "A novel source-side monitored capacitive power transfer system for contactless mobile charger using class-E converter," in *Proc. Veh. Technol. Conf.*, 2014, pp. 1–5.

[3] E. Y. Chow, "Wireless powering and the stud of RF propagation through ocular tissue for development of implantable sensors," *IEEE Trans. Antennas Propag.*, vol. 59, no. 6, pp. 2379–2387, Jun. 2011.

[4] N. Wang, Y. Zhu, W. Wei, J. Chen, S. Liu, P. Li, and Y. Wen, "One-to-multipoint laser remote power supply system for wireless sensor networks," *IEEE Sensors J.*, vol. 12, no. 2, pp. 389–396, Feb. 2012.

[5] I. Shnaps and E. Rimon, "Online coverage by a tethered autonomous mobile robot in planar unknown environments," *IEEE Trans. Robot.*, vol. 30, no. 4, pp. 966–974, Aug. 2014.

[6] S. Choi, B. Choi, S. Jeong, B. Gu, S. Yoo, and Chun T. Rim, "Tethered aerial robots using contactless power systems for extended mission time and range," in *Proc. IEEE Energy Convers. Congr. Expo.*, 2014, pp. 912–916.

[7] O. C. Onar, J. Kobayashi, and A. Khaligh, "A fully directional universal power electronic interface for EV, HEV, and PHEV applications," *IEEE Trans. Power Electron.*, vol. 28, no. 12, pp. 5489–5498, Dec. 2013.

[8] E. Waffenschmidt, "Free positioning for inductive wireless power system," in *Proc. IEEE Energy Convers. Congr. Expo.*, 2011, pp. 3481–3487.

[9] W. Zhong, X. Liu, and S. Hui, "A novel single-layer winding array and receiver coil structure for contactless battery charging systems with free-positioning and localized charging features," *IEEE Trans. Ind. Electron.*, vol. 58, no. 9, pp. 4136–4143, Sep. 2011.

[10] C. Park, S. Lee, G. Cho, S. Choi, and C. T. Rim, "Omni-directional inductive power transfer system for mobile robots using evenly displaced multiple pick-ups," in *Proc. IEEE Energy Convers. Congr. Expo.*, 2012, pp. 2492–2497.

[11] C. Park, S. Lee, G. Cho, S. Choi, and C. T. Rim, "Two-dimensional inductive power transfer system for mobile robots using evenly displaced multiple pickups," *IEEE Trans. Ind. Appl.*, vol. 50, no. 1, pp. 538–565, Jun. 2013.

[12] B. Che, G. Yang, F. Meng, K. Zhang, J. Fu, Q. Wu, and L. Sun, "Omni-directional non-radiative wireless power transfer with rotating magnetic field and efficiency improvement by metamaterial," *Appl. Phys. A*, vol. 116, no. 4, pp. 1579–1586, Apr. 2014.

[13] W. Ng, C. Zhang, D. Lin, and S. Hui, "Two- and three-dimensional omnidirectional wireless power transfer," *IEEE Trans. Power Electron.*, vol. 29, no. 9, pp. 4470–4474, Jan. 2014.

[14] H. Li, G. Li, X. Xie, Y. Huang, and Z. Wang, "Omnidirectional wireless power combination harvest for wireless endoscopy," in *Proc. Biomed. Circuits Syst. Conf.*, 2014, pp. 420–423.

[15] X. Li, T. Sun, G. Li, X. Xie, Y. Gu, and Z. Wang, "A new omnidirectional wireless power transmission solution for the wireless endoscopic microball," in *Proc. Int. Symp. Circuits Syst.*, 2011, pp. 2609–2612.

[16] R. Carta, G. Tortora, J. Thone, B. Lenaerts, P. Valdastri, A. Menciassi, P. Dario, and R. Puers, "Wireless powering for a self-propelled and steerable endoscopic capsule for stomach inspection," *Biosens. Bioelectron.*, vol. 25, no. 4, pp. 845–851, Dec. 2009.

[17] T. Sun, X. Xie, G. Li, Y. Gu, Y. Deng, and Z. Wang, "Integrated omnidirectional wireless power receiving circuit for wireless endoscopy," *Electron. Lett.*, vol. 48, no. 15, pp. 907–908, Jul. 2012.

[18] B. Lenaerts and R. Puers, "An inductive power link for a wireless endoscope," *Biosens. Bioelectron.*, vol. 22, no. 7, pp. 1390–1395, Feb. 2007.

[19] B. Choi, E. Lee, J. Kim, and C. T. Rim, "7m-off-long-distance extremely loosely coupled inductive power transfer system using dipole coils," in *Proc. IEEE Energy Convers. Congr. Expo.*, 2014, pp. 858–863.

[20] C. Park, S. Lee, G. Cho, and C. T. Rim, "Innovative 5-m-off-distance inductive power transfer systems with optimally shaped dipole coils," *IEEE Trans. Power Electron.*, vol. 30, no. 2, pp. 817–827, Nov. 2014.

[21] C. T. Rim and G. Cho, "New approach to analysis of quantum rectifier-inverter," *Electron. Lett.*, vol. 25, no. 25, pp. 1744–1745, Dec. 1989.

[22] C. T. Rim, "Unified general phasor transformation for AC converters," *IEEE Trans. Power Electron.*, vol. 26, no. 9, pp. 2465–2475, Sep. 2011.

[23] J. Huh, W. Lee, S. Choi, G. Cho, and C. T. Rim, "Frequency-domain circuit model and analysis of coupled magnetic resonance systems," *J. Power Electron.*, vol. 13, no. 2, pp. 275–286, Mar. 2013.

[24] A. Kurs, A. Karalis, R. Moffatt, J. D. Joannopoulos, P. Fisher, and M. Soljacic, "Wireless power transfer via strongly coupled magnetic resonance," *Science*, vol. 317, no. 5834, pp. 83–86, Jun. 2007.

[25] A. P. Sample, D. A. Meyer, and J. R. Smith, "Analysis, experimental results, and range adaption of magnetically coupled resonators for wireless power transfer," *IEEE Trans. Ind. Electron.*, vol. 58, no. 2, pp. 544–554, Feb. 2011.

[26] T. Imura and Y. Hori, "Maximizing air gap and efficiency of magnetic resonant coupling for wireless power transfer using equivalent circuit and Neumann formula," *IEEE Trans. Ind. Electron.*, vol. 58, no. 10, pp. 4746–4752, Oct. 2011.

[27] T. C. Beh, T. Imura, and Y. Hori, "Basic study of improving efficiency of wireless power transfer via magnetic resonance coupling based on impedance matching," in *Proc. Int. Symp. Ind. Electron.*, 2010, pp. 2011–2016.
[28] J. Park, Y. Tak, Y. Kim, Y. Kim, and S. Nam, "Investigation of adaptive matching methods for near-field wireless power transfer," *IEEE Trans. Antennas Propag.*, vol. 59, no. 5, pp. 1769–1773, May 2011.
[29] J. Huh, W. Y. Lee, S. Y. Choi, G. H. Cho, and C. T. Rim, "Explicit static circuit model of coupled magnetic resonance system," in *Proc. IEEE Power Electron. ECCE Asia Conf.*, 2011, pp. 2233–2240.
[30] E. Lee, J. Huh, X. V. Thai, S, Choi, and C. T. Rim, "Impedance transformers for compact and robust coupled magnetic resonance systems," in *Proc. IEEE Energy Convers. Congr. Expo.*, 2013, pp. 2239–2244.
[31] R. Hui, W. Zhong, and C. Lee, "A critical review of recent progress in mid-range wireless power transfer," *IEEE Trans. Power Electron.*, vol. 29, no. 9, pp. 4500–4511, Sep. 2014.
[32] G. Covic, M. Kissin, D. Kacprzak, N. Clausen, and H. Hao, "A bipolar primary pad topology for EV stationary charging and highway power by inductive coupling," in *Proc. IEEE Energy Convers. Congr. Expo.*, 2011, pp. 1832–1838.
[33] S. Li and C. Mi, "Wireless power transfer for electric vehicle applications," *IEEE Trans. Emerg. Sel. Topics Power Electron.*, vol. 3, no. 1, pp. 4–17, Mar. 2015.
[34] S. Choi, J. Huh, W. Lee, and C. T. Rim, "Asymmetric coil sets for wireless stationary EV chargers with large lateral tolerance by dominant field analysis," *IEEE Trans. Power Electron.*, vol. 29, no. 12, pp. 6406–6420, Dec. 2014.
[35] M. Budhia, G. Covic, and J. Boys, "Design and optimization of circular magnetic structures for lumped inductive power transfer systems," *IEEE Trans. Power Electron.*, vol. 26, no. 11, pp. 3096–3108, Nov. 2011.
[36] M. Budhia, J. Boys, G. Covic, and C. Huang, "Development of a single-sided flux magnetic coupler for electric vehicle IPT charging systems," *IEEE Trans. Ind. Electron.*, vol. 60, no. 1, pp. 318–328, Jan. 2013.
[37] T. Nguyen, S. Li, W. Li, and C. Mi, "Feasibility study on bipolar pads for efficient wireless power chargers," in *Proc. Appl. Power Electron. Conf. Expo.*, 2014, pp. 1676–1682.
[38] P. Meyer, P. Germano, M. Markovic, and Y. Perriard, "Design of a contactless energy-transfer system for desktop peripherals," *IEEE Trans. Ind. Appl.*, vol. 47, no. 4, pp. 1643–1651, Jul. 2011.
[39] J. Shin, S. Shin, Y. Kim, S. Ahn, S. Lee, G. Jung, S. Jeon, and D. Cho, "Design and implementation of shaped magnetic-resonance-based wireless power transfer system for roadway-powered moving electric vehicles," *IEEE Trans. Power Electron.*, vol. 61, no. 3, pp. 1179–1192, Mar. 2014.
[40] G. Elliott, J. Boys, and G. Covic, "A design methodology for flat pick-up ICPT systems," in *Proc. IEEE Conf. Ind. Electron. Appl.*, 2006, pp. 1–7.
[41] S. Lee, J. Huh, C. Park, N. Choi, G. Cho, and Chun T. Rim, "On-line electric vehicle using inductive power transfer system," in *Proc. IEEE Energy Convers. Congr. Expo.*, 2010, pp. 1598–1601.
[42] J. Huh, S. Lee, C. Park, G. Cho, and C. T. Rim, "High performance inductive power transfer system with narrow rail width for on-line electric vehicles," in *Proc. IEEE Energy Convers. Congr. Expo.*, 2010, pp. 647–651.
[43] J. Huh, W. Lee, B. Lee, G. Cho, and C. T. Rim, "Characterization of novel inductive power transfer systems for on-line electric vehicles," in *Proc. Appl. Power Electron. Conf. Expo*, 2011, pp. 1975–1979.
[44] J. Huh, S. Lee, W. Lee, G. Cho, and C. T. Rim, "Narrow-width inductive power transfer system for On-Line Electrical Vehicles," *IEEE Trans. Power Electron.*, vol. 26, no. 12, pp. 3666–3679, Dec. 2011.
[45] S. Lee, W. Lee, J. Huh, H. Kim, C. Park, G. Cho, and Chun T. Rim, "Active EMF cancellation method for I-type pickup of on-line electric vehicles," in *Proc. Appl. Power Electron. Conf. Expo.*, 2011, pp. 1980–1983.
[46] W. Lee, J. Huh, S. Choi, X. V. Thai, J. Kim, E. Al-Ammar, M. El-Kady, and Chun T. Rim, "Finite-width magnetic mirror models of mono and dual coils for wireless electric vehicles," *IEEE Trans. Power Electron.*, vol. 28, no. 3, pp. 1413–1428, Mar. 2013.
[47] S. Choi, J. Huh, W. Lee, S. Lee, and C. T. Rim, "New cross-segmented power supply rails for roadway powered electric vehicles," *IEEE Trans. Power Electron.*, vol. 28, no. 12, pp. 5832–5841, Dec. 2013.
[48] S. Lee, B. Choi, and C. T. Rim, "Dynamic characterization of the inductive power transfer system for online electric vehicles by Laplace phasor transform," *IEEE Trans. Power Electron.*, vol. 28, no. 12, pp. 5902–5909, Dec. 2013.
[49] S. Choi, B. Gu, S. Jeong, and C. T. Rim, "Ultra-slim S-type inductive power transfer system for roadway powered electric vehicles," in *Proc. Electr. Veh. Technol. Conf.*, 2014, pp. 1–7.
[50] S. Choi, B. Gu, S. Lee, W. Lee, J. Huh, Chun T. Rim, "Generalized active EMF cancel methods for wireless electric vehicles," *IEEE Trans. Power Electron.*, vol. 29, no. 11, pp. 5770–5783, Nov. 2014.
[51] C. Wang, O. Stielau, and G. Covic, "Design considerations for a contactless electric vehicle battery charger," *IEEE Trans. Ind. Electron.*, vol. 52, no. 5, pp. 1308–1314, Oct. 2005.
[52] C. Wang, G. Covic, and O. Stielau, "Power transfer capability and bifurcation phenomena of loosely coupled inductive power transfer systems," *IEEE Trans. Ind. Electron.*, vol. 51, no. 1, pp. 148–157, Feb. 2004.
[53] G. Covic and J. Boys, "Modern trends in inductive power transfer for transportation applications," *IEEE Trans. Emerg. Sel. Topics Power Electron.*, vol. 1, no. 1, pp. 28–41, Mar. 2013.
[54] O. Onar, J. Miller, S. Campbell, C. Coomer, C. White, and L. Seiber, "A novel wireless power transfer for in-motion EV/PHEV charging," in *Proc. Appl. Power Electron. Conf. Expo.*, 2013, pp. 2073–3080.
[55] S. Choi, B. Gu, S. Jeong, and C. T. Rim, "Advances in wireless power transfer systems for roadway-powered electric vehicles," *IEEE Trans. Emerg. Sel. Topics Power Electron.*, vol. 3, no. 1, pp. 18–35, Mar. 2015.
[56] B. Lee, H. Kim, S. Lee, C. Park, and C. T. Rim, "Resonant power shoes for humanoid robots," in *Proc. IEEE Energy Convers. Congr. Expo.*, 2011, pp. 1791–1794.
[57] B. Choi, E. Lee, J. Huh, and C. T. Rim, "Lumped impedance transformers for compact and robust coupled magnetic resonance systems," *IEEE Trans. Power Electron.*, vol. PP, no. 99, pp. 1, Jan. 2015, (Early access article).
[58] J. Kim, J. Kim, S. Kong, H. Kim, I. Suh, N. Suh, D. Cho, J. Kim, and S. Ahn, "Coil design and shielding methods for a magnetic resonant wireless power transfer system," *Proc. IEEE*, vol. 101, no. 6, pp. 1332–1342, Jun. 2013.
[59] J. Craig, "Spatial descriptions and transformations," in *Introduction to Robotics*, 3rd ed. Englewood Cliffs, NJ, USA: Prentice-Hall, 2004, ch. 2, sec. 8, pp. 41–51.

Bo H. Choi (S'13) received the B.S. degree in electrical engineering from Sungkyunkwan University, Suwon, Korea, in 2011. He is currently working toward the integrated master's Ph.D. degree in nuclear and quantum engineering at the Korea Advanced Institute of Science and Technology, Daejeon, Korea.

His current research interests include the power converter, wireless power transfer, magnetics, and energy grid applications.

Eun S. Lee (S'14) received the B.S. degree in electrical engineering from Inha University, Incheon, Korea, in 2012, and the M.S. degree in nuclear and quantum engineering from the Korea Advanced Institute of Science and Technology, Daejeon, Korea, in 2014, where he is currently working toward the Ph.D. degree.

His current research interests include power converter, LED drivers, and wireless power transfer.

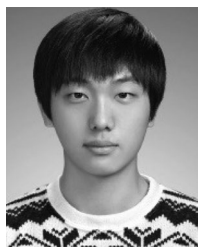

Yeong H. Sohn (S'14) received the B.S. and M.S. degrees in electrical engineering from the Korea Advanced Institute of Science and Technology, Daejeon, Korea, in 2012 and 2014, respectively, where since 2014, he has been working toward the Ph.D. degree.

His current research interests include plasma power converter, wireless power transfer, and power management IC.

Gi C. Jang (S'15) received the B.S. degree in electrical engineering from the Korea Advanced Institute of Science and Technology, Daejeon, Korea, in 2015, where he is currently working the M.S. degree in nuclear and quantum engineering.

His current research interests include power converter, LED drivers, and wireless power transfer.

Chun T. Rim (M'90–SM'11) was born in Korea, in 1963. He received the B.S. degree in electrical engineering from the Kumoh Institute of Technology, Gumi, Korea, in 1985, and the M.S. and Ph.D. degrees in electrical engineering from the Korea Advanced Institute of Technology (KAIST), Daejeon, Korea, in 1987 and 1990, respectively.

From 1990 to 1995, he was a Military Officer with the Ministry of National Defense in Korea. From 1995 to 2003, he was a Senior Researcher with the Agency for Defense Development, Daejeon, and from 1997 to 1999, he was with Astrium, Portsmouth, U.K. From 2003 to 2007, he was a Senior Director with the Presidential Office, Seoul, Korea. He was involved in developing Korea's first airborne and spaceborne Synthetic Aperture Radars. Since 2007, he has been an Associate Professor of nuclear and quantum engineering, and an Adjunct to aerospace engineering in power electronics at KAIST. He is currently developing various wireless power technologies including inductive power transfer systems for On-Line Electrical Vehicles and leading the Nuclear Power Electronics and Robots Lab (PEARL) at KAIST. He has authored or coauthored 118 technical papers, written five books, and holds more than 117 patents (awarded and pending). His research interests include wireless electric vehicles, wireless power systems for robots and biomedical applications, and general unified modeling of power electronics.

Dr. Rim received three prizes awarded by the Korean Government and has been the Chair of wireless power committee of KIPE since 2010 and the Chair of the EV charger committee of KIEE since 2011, respectively.

He is currently an Associate Editor of the IEEE TRANSACTIONS ON POWER ELECTRONICS and the JOURNAL OF EMERGING AND SELECTED TOPICS IN POWER ELECTRONICS (JESTPE), a Guest Editor of the Special Issue on Wireless Power Transfer of the IEEE TRANSACTIONS ON POWER ELECTRONICS and the JESTPE, and the general Chair of the 2014 IEEE VTC-Workshop on Wireless power (WoW) and 2015 IEEE WoW, respectively.